Skin Collagen Actively Regulates the Aging of Cutaneous Sensory Neurons

Meera Krishna[1,2], Ariel L. Franitza[2], Lezi E[1,2,*]

[1]Department of Cell Biology, Neurobiology and Anatomy, Medical College of Wisconsin, Milwaukee, WI, United States
[2]Neuroscience Research Center, Medical College of Wisconsin, Milwaukee, WI, United States

[*]Corresponding author/Lead contact: lezie@mcw.edu; Phone: 1-414-955-2248

ABSTRACT

Despite significant progress in understanding the molecular processes of aging-associated neurodegeneration, the upstream mechanisms driving neuronal aging remain elusive. Here, we investigate the potential regulatory roles of non-neural tissues in neuronal aging, using *Caenorhabditis elegans* PVD polymodal neuron as a model. We find that cutaneous PVD neurons develop progressive excessive dendritic branching during normal aging, functionally correlated with age-related deficits in proprioception. Our study reveals that age-related reduction in skin collagens, a common change across species, triggers the aging process of PVD. Specifically, loss-of-function mutations or adulthood-specific RNAi knockdown of skin collagen genes, *dpy-5* or *col-120*, which are downregulated with age, induce an early onset of PVD excessive dendritic branching and proprioception deficits. Overexpressing *dpy-5* or *col-120* mitigates the development of excessive branching without affecting lifespan, suggesting a skin collagens' role in promoting healthspan rather than longevity. Notably, neither *dpy-5* or *col-120* is not involved in aging-associated dendritic beading, another degenerative phenotype in PVD associated with harsh touch response deficits. Moreover, *dpy-5* mutation induces ectopic branching in ALM, but does not affect PLM, two other cutaneous sensory neurons. Finally, we identify *rig-3*, a neuronal Immunoglobulin Superfamily member not expressed in PVD or the skin, functioning in the same pathway as skin collagen genes to preserve PVD neuron integrity during aging. Our findings reveal the causative role of age-related reduction in skin collagens in neuronal aging, selectively impacting distinct neuron subtypes and structures. This study underscores the importance of exploring multi-tissue strategies to comprehensively address the complexities of neuronal aging.

INTRODUCTION

Age represents a significant risk factor for many neurological disorders, including peripheral neuropathies [1-4]. While several factors such as diabetes, autoimmune diseases, physical injury, and vitamin imbalances can contribute to neuropathies, aging not only increases susceptibility to these conditions but also raises the prevalence of idiopathic neuropathies [2,5,6]. Currently, our ability to treat neuropathies in elderly populations is limited, largely due to gaps in our understanding of the mechanisms driving aging of the nervous system. Signaling from non-neural tissues is one potential avenue in this regard.

It is well documented that development of the nervous system is highly dependent on appropriate signaling from adjacent non-neural tissues. Vascular smooth muscle cells in the brain, for example, secrete factors such as thrombospondin, a known synaptogenic factor, to promote neurite formation in mouse hippocampal neuronal cultures [7]. Proper expression of neurotrophic factors in the skin is also crucial for guiding peripheral sensory innervation, as demonstrated by studies showing that overexpression of neurotrophin-4 in the epidermal basal cells of mice leads to abnormally increased innervation of the dermal footpad [8-10]. In *C. elegans*, the morphogenesis of the PVD neuron, a cutaneous sensory neuron with an elaborate dendritic arbor similar to typical mammalian sensory neurons, relies on the cell-adhesion molecule SAX-7 on the skin, along with several other extracellular proteins, to serve as precise tracks for accurate dendritic arborization [11-14]. In *Drosophila* and zebrafish, epidermal ensheathment, a process where epidermal cells wrap around growing neurites of cutaneous sensory neurons to regulate branching morphogenesis, is also highly dependent on two-way signaling between the neuron and the skin; blocking epidermal sheath formation in these models results in destabilized dendrite branches and reduced nociceptive function [15]. Together, the evidence emphasizes the critical role of non-neural tissues in the proper development of peripheral nerves. However, whether non-neural tissues also actively contribute to the aging of peripheral nervous system remains less understood.

During aging, neurons undergo progressive structural deterioration, leading to increased synapse loss and impaired neuronal signal transmission, ultimately resulting in a variety of behavioral abnormalities [16-19]. Neuritic beading, also known as focal swelling, is a common aging-associated structural change indicative of neurodegeneration. It is characterized by beads-on-a-string-like structures along neurites and is evolutionarily conserved across organisms from *C. elegans* to mice to humans [20,21]. These neuritic beads, consisting of broken-down cytoskeletal and motor protein components, can disrupt organelle transport, such as mitochondrial trafficking, leading to bioenergetic dysfunction and eventual neuronal death [20,22]. Our previous research in *C. elegans* has shown that age-related upregulation of antimicrobial peptides in the skin causatively triggers dendritic beading in PVD neurons accompanied by a functional decline, demonstrating a significant role for skin-derived molecular cues in sensory neuron aging [23].

Increased aberrant neurite branching is another aging-associated structural change in neurons, documented in the peripheral nervous systems of aged rats and elderly human patients with sensory neuropathies [24-26]. While it has been speculated that the increased branching may compensate for other aging-associated structural and functional losses, this counterintuitive phenomenon is not well

understood. Interestingly, *C. elegans* PVD neurons also exhibit a pronounced increase in dendritic branching at advanced ages, as briefly mentioned in our prior work [23] and also observed in a separate study by Kravtsov et al [27], though the functional implications and precise underlying mechanisms remain unknown. However, it is noteworthy that the aging-associated excessive branching, unlike the dendritic beading, does not appear to be regulated by skin antimicrobial peptides, suggesting the involvement of alternative mechanisms.

In this study, we provide a comprehensive characterization of aging-associated excessive dendritic branching in PVD neurons, demonstrating its functional relevance to age-related decline in proprioception. Using PVD neuron as a model, we further discover that mutations or downregulation of two skin collagen genes, *dpy-5* and *col-120*, induce early-onset excessive dendritic branching and proprioceptive deficits, suggesting that age-dependent reduction of skin collagens plays a causative role in sensory neuron aging. Moreover, overexpression of these collagen genes mitigates the severity of excessive branching in old animals, highlighting their neuroprotective effects in aging. Importantly, our results also indicate that the regulatory role of skin collagens is specific to branching integrity during aging and is limited to certain types of cutaneous sensory neurons. Additionally, we identify neuronal RIG-3, an Immunoglobulin Superfamily protein, as a co-factor participating in skin collagen's regulation of PVD dendritic integrity. These findings reveal a novel role for skin collagens in actively regulating sensory neuron aging, expanding our understanding of the upstream molecular mechanisms that drive nervous system aging.

RESULTS

Aging triggers the progressive development of excessive higher-order dendritic branching in PVD sensory neurons

To investigate how skin tissues may affect the aging of sensory neurons, we employed the PVD neuron of *C. elegans* as our experimental model. The PVD neuron is a cutaneous multi-dendritic mechanosensory neuron that spans the entire body of the animal along the anterior-posterior axis excluding the head, neck, and tail [28,29]. Functionally, the PVD is involved in harsh touch sensation, cold sensation, and proprioception [30,31]. Each animal possesses two PVD neurons, PVDR on the right and PVDL on the left [32,33]. The dendritic branches of the PVD neuron extend dorsally and ventrally, with a singular axon that synapses ventrally with the AVA and PVC interneurons (Fig. 1A) [32-34]. From the PVD soma, two primary (1º) dendritic branches extend in the anterior and posterior directions, respectively, with secondary (2º) dendrites emerging orthogonally from the 1º dendrites at regular intervals, forming non-overlapping 'menorah-like' repeating units mainly composed of tertiary (3º) and quaternary (4º) dendrites (Fig. 1B) [29,33,35]. The normal aging process of PVD neurons, as previously investigated by our group and others [23,36], often involves the progressive development of bead-like structures along the dendrites (Fig. S1A), resembling morphological changes observed in human patients with peripheral neuropathies or mammalian models of age-related neurodegenerative diseases [37-42]. We have demonstrated that the majority of the beading structures in PVD dendrites indicate a disrupted

microtubule network and are associated with age-related deficits in the harsh touch sensing function of PVD neurons (Fig. S1B) [23].

In this study, we focused on another distinctive aging phenotype of PVD neurons – excessive dendritic branching, previously noted in literature [23,27] yet lacking clarification regarding its functional implications and underlying mechanisms. We first conducted a thorough characterization of this phenotype. Our examination throughout the normal aging process of control animals [*wdIs51* (*F49H12.4::GFP)*] revealed a progressive and substantial increase in the number of 5º and 6º dendritic branches from Day 1 to Day 9 of adulthood (Fig. 1C-E, Fig. S1C-F), while the number of 4° dendrites or PVD menorahs remained unchanged (Fig. S1G-N). Notably, no age-related ectopic branching was detected in the axons. To ascertain whether the observed excessive dendritic branching is an inherent consequence of aging, we pursued a different approach from the common method of disrupting specific aging signaling pathways, such as *daf-2* signaling [43]. Instead, we leveraged the well-established correlation between environmental temperatures and the aging process in *C. elegans*. Previous studies have demonstrated that higher temperatures accelerate aging, while lower temperatures decelerate it, potentially involving multiple signaling pathways [44-48]. Our findings revealed a temperature-dependent variation in the severity and progression of PVD dendritic branching (Fig. 1F-G), suggesting that this morphological change is an intrinsic aspect of aging. Furthermore, to adjust for the slight increase in body size observed during aging, our analysis indicated that the significant increase in branching persisted even after normalizing for the animal's body length (Fig. S1W-X), further reinforcing the relevance of this phenotype to aging. Kravtsov et al. previously showed that *daf-2* mutant animals exhibited increased 5°-7° dendritic branches in PVD neurons to a similar extent as control animals of the same advanced ages [27], implying that the intrinsic aging nature of this morphological change we demonstrated here is independent of the insulin/IGF-1 pathway but potentially involves other aging signaling pathways.

Upon conducting a more in-depth analysis of the aging-associated higher-order (≥ 5°) dendritic branching, we observed that its extent and progression were comparable between left and right PVD neurons throughout aging (Table S1). While slight variations were noted in the number of higher-order branches when comparing the dorsal and ventral sides of PVD neurons, the overall aging-associated trend remained evident in both sides (Fig. S1C-F). Importantly, this trend persisted even after normalization for the number of PVD 'menorah' structures or 4° dendritic branches (Fig. 1H-K, Fig. S1O-R). Furthermore, using the position of the PVD soma as a dividing point, we compared between the anterior and posterior sections. Following a similar normalization approach, although the extent of high-order branching per PVD 'menorah' or per 4° dendritic branches in the posterior section was notably greater than that in the anterior section of the same PVD neuron across ages, the aging-associated increase trend was observed in both sections (Fig 1L-O, Fig. S1S-V).

During development, stabilized microtubules are often found in large primary dendrites, while actin is abundant in small higher-order dendrites or dendritic spines, playing a crucial role in anatomical plasticity [49,50]. To determine the cytoskeletal composition of the aging-associated higher-order dendritic branches of PVD neurons, we used transgenic strains expressing *ser-2(3)p::EMTB::GFP* (microtubule-

binding domain of ensconsin fused to GFP) or *ser-2(3)p::GFP::UtrCH* (calponin homology domain of F-actin binding protein utrophin fused to GFP) to visualize polymerized microtubules or actin filaments, respectively, in PVD neurons [23,51-55]. We found that microtubules were not detectable in >3° dendritic branches in aged control animals (Fig. S2A), similar to the microtubule distribution pattern in young adults [56]. In line with previous reports [55], our time-lapse imaging analysis of young adult control animals showed abundant localization of F-actin in 4° dendrites and the leading edges of occasional higher-order dendritic branches (Fig. 1P, Fig. S2B). Interestingly, the excessive 5°/6° dendrites in aged control animals primarily consisted of F-actin as well (Fig. 1P, Fig. S2B). Further quantitative analysis of our time-lapse imaging data indicated dynamic remodeling of F-actin-rich higher-order branches in both young and aged control animals, with frequent outgrowths and retractions over minutes (Fig. 1Q-R). Notably, within the same observation period, higher-order branches in aged control animals tended to gain length, while those in young adults appeared prevented from further growth (Fig. 1S). Given the crucial role of pruning or phagocytosis in neural network refinement during development [57], it is plausible that this process also contributes to the dynamic remodeling of higher-order branches during adulthood. In *C. elegans*, both epidermal cells and body wall muscles can take on amateur phagocytic roles [58,59]. Typically, phagocytosis results in the presence of cellular debris in the vicinity. However, we did not observe such debris near the remodeled regions, which would theoretically be visible as fluorescent puncta [60], suggesting that the dynamic remodeling of PVD higher-order branching is unlikely to occur through phagocytosis. Importantly, we did not observe abnormal overlapping of dendritic branches when excessive higher-order branching developed during aging. Previous studies have shown that manipulation of several genes that regulate PVD dendrite self-avoidance, such as *mig-14*/Wntless and *eff-1*/fusogen, affects 2°-4° branching but does not seem to affect higher-order branches [27,29,61], suggesting that the observed phenotype in our study is also independent of dysregulated self-avoidance between sister dendrites. Collectively, these findings hint at potential alternative regulatory mechanisms that effectively preserve dendritic branching integrity in young adults but may be compromised in aged individuals.

Aging-associated excessive dendritic branching in PVD neurons correlates with proprioceptive deficits

We next investigated the potential functional implications of the excessive branching observed in aging PVD neurons. Harsh touch sensation is a well-studied function of PVD neurons; this function relies on their proper synaptic connections with downstream command interneurons that further integrate signals into motor neuron circuits to initiate an escape movement [31,62]. To examine the relevance of excessive PVD dendritic branching in dysfunctional harsh touch sensation, we first performed the behavioral analysis of noxious harsh touch response [23,31], followed by the examination of the dendrite morphology of the same animal, enabling a within-individual analysis of the correlation between the dendritic structure deterioration and sensory deficits. Interestingly, our findings showed that age-dependent decline of harsh touch response in control animals [23] had no correlations with the extent of PVD higher-order dendritic branching (Fig. S3A), as opposed to the strong positive correlation with aging-associated dendritic beading phenotype (Fig. S1B).

As a polymodal neuron that responds to several distinct sensory modalities besides harsh touch, the integrity of PVD dendritic menorah structures has specifically been shown to be critical in providing proprioceptive regulation, without relying on PVD axons' synaptic function [30,63]. Proprioception refers to the ability to process sensorimotor input for posture control and precise movement output; with *C. elegans*, it can be assessed by measuring the tracks that the animals leave on agar plates seeded with *Escherichia coli* OP50 (standard food in laboratory maintenance), through their sinusoidal body-bend movements (Fig. 2A) [64]. Animals harboring a loss-of-function mutation in *dma-1* or in several other genes that lead to impaired morphogenesis of PVD menorah structures (marked by the absence of dendritic arborization beyond 2° branches) exhibit a decrease in track wavelength and amplitude [30]. We therefore hypothesized that the excessive higher-order dendritic branching in aging PVD neurons could manifest as proprioceptive deficits at the behavioral level.

To test our hypothesis, we first examined the proprioceptive function in control (CT) animals during aging. Compared to young Day 3 animals, we observed a significant decrease in the mean amplitude and mean wavelength of the sinusoidal movements in aged Day 9 animals (Fig. 2B-C). Additionally, there was a notable increase in within-individual variability in the wavelength of tracks in Day 9 animals, accompanied by a trend towards increased variability in amplitude as well (Fig. 2D-E). These age-related changes resemble the gait pattern changes observed in elderly humans, such as decreased stride length/width and greater variability in these parameters, which are strongly associated with a decline in proprioception [65-68]. To further examine the relevance of excessive PVD dendritic branching in the age-related proprioceptive deficits, we then conducted a within-individual correlation analysis between branching severity and proprioceptive function (Fig. 2, Fig. S3). Our analysis revealed that the extent of 'higher-order' branches, dorsal 6° branches in particular, was negatively correlated with the mean amplitude or mean wavelength (Fig. 2F-G). On the other hand, the severity of dorsal 6° branches was positively correlated with the variability in track amplitude or wavelength (Fig. 2H-I). Subsequent examination of PVD dendritic beading and excessive branching within individual animals revealed an absence of concurrence of these two aging-related phenomena; rather, a negative correlation seems evident, wherein animals exhibiting a pronounced beading phenotype are less likely to exhibit severe branching, and vice versa (Fig. S3V-W). This observation, coupled with our finding regarding the distinct behavioral manifestations of dendritic beading and excessive branching [23] (Fig. 2, Fig. S1B, Fig. S3), hints at the existence of a potential compensatory mechanism aimed at preserving certain functions of polymodal neurons. Collectively, we established a novel link between aging-associated excessive branching of PVD dendrites and age-related proprioceptive deficits. Our findings further imply that neurons may undergo a variety of morphological changes during aging, each leading to unique functional consequences.

Loss-of-function mutations in skin collagen genes lead to an early onset of excessive PVD dendritic branching and proprioceptive deficits.

In our previous research, we identified a skin antimicrobial peptide (AMP) as a factor contributing to PVD dendritic beading; interestingly, this factor does not explain the phenomenon of aging-associated excessive dendritic branching [23]. However, it does suggest that age-related changes in the skin can

influence the aging of PVD neurons, which motivated us to explore whether other molecular changes in the aging skin could play a role in the observed excessive branching. A prime candidate for such a role is the age-related decline in skin collagen gene expression (Fig. S4A) [69], a phenomenon well-documented in various organisms, including rodents and humans [70-73].

In *C. elegans*, the skin comprises a simple epithelium known as the epidermis or hypodermis [74]; this epithelial layer secretes a collagenous cuticle to the apical side, serving as an additional protective barrier [75,76]. Our exploration into the downregulation of skin collagen genes during aging led us to discover that null mutations in either *dpy-5* or *col-120* resulted in an early-onset of the excessive PVD dendritic branching by Day 3 of adulthood, comparable to the branching severity observed in much older control animals (Fig. 3A-G). Despite lacking direct mammalian orthologs, DPY-5 and COL-120 share a similar domain architecture with mammalian membrane-associated or fibril-associated collagens with interrupted triple-helices (Fig. 3A)[77-79]. The expression of *dpy-5* and *col-120* are not temporally clustered, and their proteins localize to distinct areas within the epidermis [80-82], suggesting that they likely do not interact functionally. Importantly, DPY-5 and COL-120 protein levels both decrease with age in wild-type animals [81,82]. Although mutations in either *dpy-5* or *col-120* do not compromise the skin integrity of the animals [83,84], both genes affect body size. *dpy-5 (e907)* mutants are noticeably shorter and wider [82,84], while *col-120 (sy1526)* mutants appear slightly elongated (Fig. S4C). In addition, both mutants exhibited reduced lifespans (Fig. S4D), suggesting a broader impact on organismal health, potentially due to developmental anomalies. To mitigate the confounding influence of body size changes on our analysis, we normalized dendritic branching to the body length of individual animals. This normalization confirmed that *col-120 (sy1526)* mutants exhibited early-onset 'higher-order' dendritic branching at Day 3, even when adjusted to body size (Fig. S1W-X).

To further solidify the specific role of skin collagens in this phenotype, we performed rescue experiments. The expression of wild-type *dpy-5* cDNA under the control of an epidermis-specific promoter successfully rescued the excessive dendritic branching phenotype in *dpy-5 (e907)* mutants at Day 3 (Fig. 3D-E, additional rescue line in Fig. S4E-F). A similar rescue effect was observed when wild-type *col-120* cDNA was expressed using epidermis-specific promoters in *col-120 (sy1526)* mutants (Fig. 3F-G, additional rescue line in Fig. S4G-H). PVD neurons complete their dendritic arborization around the late L4 stage (last/4th larval stage) [33,85,86]. Examination of *dpy-5* and *col-120* mutant animals at the L4 stage revealed a slight increase in excessive dendritic branching compared to control animals, though not reaching the extent observed in Day 3 mutant animals (Fig. S4I-J). To determine whether the excessive dendritic branching observed in *dpy-5* or *col-120* mutants arises from developmental defects or is genuinely associated with aging, we performed adulthood-specific systemic RNA interference (RNAi) knockdowns of these genes. We used the feeding method, where *E. coli* HT115(DE3) carrying either the empty L4440 double T7 vector or the vector producing dsRNA for the gene of interest is fed to *C. elegans* as food [87]. RNAi treatment was initiated at the late L4 stage to avoid interfering with PVD dendritic morphogenesis, and phenotyping was performed 3 days later (Day 3 of adulthood). The effectiveness of adulthood RNAi was validated through RT-qPCR analysis (Fig. S4B). We first confirmed that control animals fed on HT115(DE3) bacteria harboring empty vector L4440 (EV, used as a negative control in RNAi assays) exhibited aging-associated excessive dendritic branching in PVD

neurons as well (Fig. S4K-L), to a similar extent as observed in control animals fed on OP50. Our data show that a modest suppression of *col-120* or *dpy-5* expression via the adulthood-specific RNAi approach was sufficient to induce excessive higher-order branches at Day 3 (Fig. 3H-K). This effect was confirmed using an additional RNAi clone we constructed to target a different coding region for each gene (Fig. S4M-P).

Importantly, we found that Day 3 *col-120 (sy1526)* mutants exhibited a significant decrease in both mean wavelength and mean amplitude of their sinusoidal movement, remarkably similar to that observed in control Day 9 animals, albeit without affecting the variability in these parameters (Fig. 3L-N, Fig. S4Q-R). Collectively, these results indicate that skin collagens, DPY-5 and COL-120, play a critical role in regulating the PVD dendritic branching integrity and PVD-navigated proprioceptive function, especially in aging. This suggests that the age-dependent reduction of skin collagens may actively contribute to the aging of cutaneous sensory neurons at both morphological and functional levels.

Overexpression of skin collagen genes delays the onset of aging-associated excessive PVD dendritic branching.

We further examined the impacts of overexpressing *dpy-5* or *col-120* in control animals to solidify their aging-associated roles in maintaining PVD dendritic branching integrity. Using the *col-19* promoter [88] we induced the overexpression of *dpy-5* in the epidermis specifically during adulthood. Our data indicate that adulthood-specific overexpression of *dpy-5* effectively mitigated excessive dendritic branches when examined at Day 9 of adulthood (Fig. 4A-B). Similar positive effects were also observed with ubiquitous overexpression of *col-120* (Fig. 4C-D; additional overexpression line in Fig. S5A-B). Moreover, epidermal overexpression of *dpy-5* appeared to shift proprioceptive function parameters in Day 9 animals towards those of a younger age, as evidenced by a trend towards increased mean wavelength and amplitude in their movement tracks, though this did not reach statistical significance (Fig. S5D-G). It is important to acknowledge that age-related declines in other systems, such as muscles and motor neurons, may complicate the assessment of the sensory aspect of proprioception at this stage of life. Interestingly, using the same overexpression strategy we found that neither *dpy-5* nor *col-120* significantly affected lifespan (Fig. 4E, Fig. S5C). While previous studies have reported a slight lifespan extension with *col-120* overexpression [89], discrepancies with our results may be attributed to differences in the promoters and 3'UTR sequences used to construct transgenic strains. Nevertheless, our findings suggest that the observed aging-associated neuroprotective effects of skin collagen are distinctly targeted towards neuronal integrity, rather than through promoting longevity.

DPY-5 and COL-120 are not involved in aging-associated dendritic beading in PVD neurons.

To investigate whether skin collagen genes regulate the overall aging of PVD neurons, we examined the effects of *dpy-5* or *col*-120 mutation on the previously documented aging-associated dendritic beading phenotype (Fig. S1A) [23,36]. Notably, the extent of PVD dendritic beading in Day 3 *dpy-5 (e907)* or *col-120 (sy1526)* mutant animals was comparable to that observed in age-matched controls (Fig. 5A).

Coupled with our observations of a potential inverse relationship between aging-associated dendritic beading and excessive dendritic branching in older control animals (Fig. S3V-W), these results suggest that *dpy-5* and *col-120* regulate PVD dendritic structure via mechanisms separate from those leading to the dendritic beading degenerative phenotype, such as the skin antimicrobial peptide NLP-29 [23]. This is also supported by previous research showing that mutations in *dpy-5* and *col-120* do not impact *nlp-29* expression [90,91]. Collectively, our findings support the notion that distinct non-neural molecular mechanisms may be underlying different dimensions of neuronal aging, even within a certain neuron sub-type.

ALM sensory neurons exhibit ectopic branching in response to *dpy-5* loss-of-function mutation, but PLM neurons do not.

To determine whether the regulatory role of skin collagens in neuron structural integrity is specific to certain neuron sub-types we examined the effects of *dpy-5* mutation on two additional sets of cutaneous sensory neurons in *C. elegans*: the ALM and PLM touch receptor neurons, which are crucial for the perception of gentle touch [92]. Intriguingly, Day 3 *dpy-5 (e907)* mutant animals exhibited an increase in ectopic, aberrant branching from ALM anterior neurites when compared to Day 3 control animals, while PLM neurons showed no morphological abnormalities (Fig. 5B-D). This discrepancy indicates that the regulatory role of skin collagens in neuritic branching may not extend uniformly across all cutaneous sensory neurons, suggesting that certain neuron sub-types may possess unique features rendering them particularly vulnerable to the effects of skin collagen loss during aging.

RIG-3/IgSF functions along with skin collagens to regulate aging-associated excessive PVD dendritic branching

We next explored the potential mechanism by which skin collagen genes regulate PVD dendritic branching during aging. In the developing nervous system, a variety of transmembrane and extracellular proteins are crucial for facilitating adhesive interactions that are critical to neuronal shape remodeling and migration [93,94]. Proteins such as SAX-7/L1CAM, MNR-1, DMA-1 (transmembrane LRR protein), and UNC52/perlecan have been extensively studied in relation to PVD dendritic morphogenesis [11,14]. Yet, it is unlikely that these elements contribute to the aging-associated increase in PVD higher-order dendritic branching. This is because SAX-7 primarily guides the extension of 1º dendrites as well as the outgrowths of 2º - 4º branches, which is also supported by the evidence showing SAX-7's epidermal localization aligning with 1º- 4º dendrites but not with higher-order branches [95,96]. Similarly, DMA-1 overexpression only induces aberrant dendritic branching at 3º level [11,85]. We therefore hypothesized that different cell adhesion molecules might play a role in aging-associated excessive branching due to loss of skin collagens.

First, we conducted a targeted RNAi screen in adulthood, focusing on several cell-cell adhesion molecules that could potentially interact with collagen, including integrins, discoidin domain receptors, and immunoglobulin-like proteins [77] (Fig. 6A-B, Fig. S6A-B). Our findings revealed that knockdown of *ina-1* (codes for an integrin alpha-subunit) or *rig-3* (codes for a protein of the Immunoglobulin

Superfamily/IgSF) led to early-onset excessive dendritic branching in PVD neurons. Unlike the widespread expression of *ina-1* in various tissues, *rig-3* is distinctly expressed, primarily in a select group of neurons, predominantly in AVA interneurons and notably not detectable in PVD, ALM, or PLM neurons [97-99]. Considering RIG-3's presumed absence in PVD, and PVD's synaptic connections with AVA, RIG-3 emerges as a compelling candidate for further investigation into its potential non-cell-autonomous role in PVD dendritic branching. Our analysis of *rig-3(ok2156)* loss-of-function mutant animals confirmed our initial findings from RNAi experiments (Fig. 6A-D). To investigate the role of *rig-3* in the regulation of PVD excessive branching by skin collagens, we performed adulthood RNAi knockdown of *rig-3* in *col-120* or *dpy-5* mutant animals. Remarkably, *rig-3* RNAi-treated *dpy-5(e907)* or *col-120(sy1526)* mutant animals did not exhibit further excessive branching when compared to empty vector-treated mutants, suggesting that *rig-3* functions in the same genetic pathway as *dpy-5* or *col-120* in regulating PVD dendritic integrity during aging (Fig. 6E-F).

To gain further insight into the downstream mechanisms of skin collagen genes in regulating PVD dendritic integrity, we analyzed publicly available microarray data (GSE19310) comparing N2/WT and *dpy-10(e128)* mutant animals at young adult stage [100]. *dpy-10* is another skin collagen gene downregulated with age (Fig. S4A), and importantly *dpy-10(e128)* mutants also exhibit early-onset excessive dendritic branching in PVD neurons (Fig. S6C-D), similar to *dpy-5* and *col-120* mutant animals. Intriguingly, the KEGG pathway analysis of the differentially expressed genes from the datasets (GSE19310) showed that the Wnt signaling pathway was among the top downregulated pathways *in dpy-10(e128)* animals compared to WT animals (Fig. S6E). Wnt signaling is well-documented to play a crucial role in guiding dendritic morphogenesis during development, controlling branch point selection, and limiting dendritic expansion into non-permissive territories [101]. While the specific involvement of Wnt signaling in the PVD phenotype studied here remains unknown, it is noteworthy that extracellular RIG-3 has been shown to restrict postsynaptic plasticity and neuronal polarity during development by interacting with a Wnt receptor in a non-cell-autonomous manner [98,102]. Given the absence of *rig-3* expression in the epidermis or PVD neurons [97,103], it is plausible to suggest that RIG-3, potentially operating from adjacent neurons such as AVA [32-34], may serve as an intermediary to relay signals from skin collagens to PVD neurons, possibly through Wnt signaling, a pathway known for its capacity to signal in a retrograde manner [104]. While future investigations are required to elucidate the order of gene action, our findings collectively demonstrate the crucial role of skin collagens in regulating sensory neuron integrity during aging, potentially mediated through a series of cellular communication processes involving cell adhesion molecules with signaling functions.

DISCUSSION

In this study we have identified a novel role for skin collagens in regulating the aging of cutaneous sensory neurons, using *C. elegans* as a model organism. Specifically, we demonstrate that loss of function mutations in non-basement membrane collagens, namely *dpy-5* or *col-120*, lead to an early-onset of aging-associated excessive dendritic branching in PVD neurons. Moreover, we further confirm the neuroprotective capacity of these skin collagens, as their overexpression significantly prolongs the integrity of dendritic structures in PVD neurons over aging. In-depth analysis reveals that the excessive

dendritic branching associated with aging in PVD neurons is strongly and distinctly correlated with proprioceptive deficits typically observed in aged wild-type animals. Notably, young adult animals with a *col-120* loss of function mutation exhibit proprioceptive deficits similar to those observed in older WT animals, providing further evidence of the critical regulatory role skin collagens play in sensory neuron aging at both morphological and functional levels. Our results also emphasize the selective impact of skin collagens on the aging of sensory neurons. This selectivity is evident at two distinct levels: firstly, skin collagens appear not to contribute to the development of neuritic beading in aging PVD neurons, pointing to a phenotype-specific effect; secondly, their role is confined to maintaining the branching integrity of specific types of cutaneous sensory neurons, highlighting a targeted cell-cell communication at the neuron sub-type level. Additionally, our genetic studies indicate that the neural cell adhesion protein RIG-3/IgSF, which is not expressed in PVD neurons or the skin, acts as a potential intermediate effector of skin collagens in preserving dendritic integrity in PVD neurons during aging. This suggests that the role of skin collagens likely extends beyond merely providing direct structural support to neurons and may be mediated through a series of complex cellular communication processes. Taken together, our study highlights the possibility that various molecular cues from non-neural tissues during aging may activate distinct mechanisms, inducing specific morphological changes in neurons that lead to unique functional consequences. This underscores the need for a paradigm shift towards exploring multi-tissue strategies to comprehensively address the complexities of neuronal aging.

Despite the significant age-related decline in the production of many collagen proteins in various tissues [70-73], research into the interactions between collagen and the nervous system during aging remains limited. Notably, one study found that mice lacking the ubiquitously expressed microfibrillar collagen VI gene, COL6A1, exhibited more severe deficits in motor coordination and spatial memory, along with increased apoptosis observed at the cellular level, when compared to WT animals of the same advanced age [105]. Our current study further provides crucial evidence that non-basement membrane collagens from non-neural tissues, such as the skin, also play a regulatory role in neuronal aging. The two collagens we examined, DPY-5 and COL-120, are skin cuticular collagens exclusive to nematodes but share structural similarities with vertebrate membrane-associated or fibril-associated collagens with interrupted triple helices, known to play key roles in collagen fibril organization [78,79]. However, the specific molecular mechanisms through which collagen non-cell-autonomously affects the aging of sensory neurons still require clarification. Our previous research has demonstrated that the epidermally-expressed antimicrobial peptide, neuropeptide-like protein 29 (NLP-29), triggers aging-associated dendritic beading in *C.* elegans PVD neurons through its interaction with a neuropeptide receptor, NPR-12, which then activates an autophagy-mediated neurodegeneration signal [23]. Similarly, neurotrophin 3 (NT3), which is downregulated in the skin with age, has been observed to affect cutaneous nerve innervations in mice during aging, likely due to diminished signaling between NT3 and its neuronal receptor, trkA [106]. Together, the evidence from these studies supports our hypothesis that collagens produced from non-neural cells or tissues may functionally interact with specific neuronal receptors or cell-surface molecules, actively contributing to the preservation of neuronal integrity during aging.

Cell-adhesion molecules are well-documented for their pivotal role in the spatial development of the nervous system across various organisms [93,94]. In *C. elegans*, cell adhesion molecules including SAX-7

and DMA-1 are integral for the dendritic morphogenesis of PVD neurons [11,14,96], though these molecules do not seem to be involved in PVD dendritic morphological changes with aging, as discussed above. Our study takes a step forward by identifying neuronal RIG-3/IgSF as a collaborator with skin collagens in modulating dendritic branching specifically during adulthood, highlighting the critical role of cell adhesion molecules in both neural development and structural changes in aging neurons. RIG-3 shares sequence homology with mammalian neural cell adhesion molecule 1(NCAM1), also a member of the IgSF [98]. Studies in a rat sciatic nerve injury model have shown that the presence and stability of NCAM1 on the axonal membrane are necessary for proper axonal fasciculation during nerve regeneration, requiring the physical interaction between extracellular collagen VI and the fibronectin type III (FNIII) domain of NCAM1 [107]. While RIG-3 also contains a FNIII domain [98], whether it directly interacts with COL-120 or DPY-5 in regulating PVD dendritic integrity remains to be determined. Intriguingly, based on the distinct expression pattern of *rig-3* in wild-type animals [97-99], it appears that RIG-3 may not directly function on the surface of the PVD neurons to receive cues from skin collagens, but potentially from nearby neurons, such as AVA or PVC interneurons, which the PVD neuron synapses onto [108]. This points to an intricate model involving multiple layers of intercellular communication to explain the bridging mechanisms between skin collagens and sensory neuron health in aging.

Excessive branching in peripheral neurons triggered by aging appears to be an evolutionarily conserved phenomenon. Studies show that wild-type rats aged between 25 to 28 months exhibit an abrupt increase in the motor neuron terminal branches at the diaphragm and leg muscles compared to younger rats, with this increase diminishing at later ages [26]. Similarly, older human subjects with sensory neuropathy exhibit increased epidermal nerve fiber branching at the proximal thigh compared to healthy control subjects [24]. In our study, time-lapse imaging revealed that the excessive high-order dendritic branches in PVD neurons are enriched with F-actin and devoid of microtubules, indicating their highly dynamic potential. Notably, this cytoskeletal makeup and dynamic behavior resemble features of dendritic spines [109], the changes in number or structure of which may lead to changes in neuronal activity or synaptic plasticity [110,111]. While it is tempting to speculate that the increased branching observed in the aging nervous system represents a compensatory plasticity for future neurodegeneration at more advanced ages, this speculation relies on understanding the functional significance of these excessive branches, especially considering that PVD dendrites are not known to form synapses with other neurons.

Our study uncovered that excessive higher-order branches in aging PVD neurons are functionally relevant to proprioceptive deficits observed during normal aging. Proper proprioception in young healthy *C. elegans*, particularly in the form of their sinusoidal movements, is largely mediated by a heterotrimeric mechanosensitive sodium channel consisting of MEC-10, UNC-8, and DEL-1, localized to the lower-order dendritic branches of PVD neurons [30]. Upon proprioceptive stimuli, this channel is activated to induce local Ca2+ increase and dendritic release of the neuropeptide NLP-12, which directly modulates the neuromuscular junctions to regulate movement vigor [30]. Further investigation is necessary to determine whether the distribution of the sodium channel in PVD dendrites and/or the release pattern of NLP-12 are altered during aging, potentially contributing to the age-related proprioceptive deficits relevant to excessive PVD dendritic branching. Such investigations may also yield insights into whether

aging-associated excessive branching in the peripheral nervous system represents aberrant compensatory plasticity that is engaging sensorimotor networks inappropriately.

Using *C. elegans* PVD neuron as a model, we demonstrate that a polymodal sensory neuron can develop more than one distinct morphological change during aging, with each type of change corresponding to a decline in a specific neuronal function. Our findings further indicate that the simultaneous occurrence of excessive dendritic branching and dendritic beading in a single animal is rare during normal aging. Therefore, it is unlikely that an animal would experience a significant decline in both harsh touch function and proprioception simultaneously. The question of whether polymodal neurons are programmed to prioritize one function over another remains unanswered. Nevertheless, our previous research [23] and current study together provide evidence intriguingly suggesting that within the same multifunctional neuron, there is a degree of selectivity regarding which structure and function are more vulnerable to the aging process, and that this selectivity is likely mediated by distinct non-neural signals.

On a broader level, neurons in different regions of the nervous system exhibit varying susceptibility or resistance to aging as well, leading to differences in the timing and pace of neurodegenerative processes. This phenomenon, known as selective neuron vulnerability, is commonly observed in both normal aging and age-related neurodegenerative diseases [112,113], though the underlying basis of this selectivity remains elusive. Importantly, this selectivity appears to be evolutionarily conserved, and is also observed in *C. elegans* ALM, PLM, and PVD neurons [23,114,115], which were the focus of our study. These neurons not only begin aging at different times and rates but also respond differently to the same skin-derived molecular cue, as demonstrated in our study. Given that each neuron class/subtype has a distinct gene expression pattern [97,116,117], future research is needed to investigate whether the unique cell surface molecular signatures of each subset of neurons play a critical role in determining which non-neural or extracellular aging signals they receive, thus creating such selectivity.

CONFLICT OF INTEREST

The authors declare that the research was conducted in the absence of any commercial or financial relationships that could be construed as a potential conflict of interest.

FUNDING SUPPORT

This work was supported by the Imagine More Award and Research Affairs Committee at the Medical College of Wisconsin, as well as Advancing a Healthier Wisconsin (AHW) Endowment project 5520482 titled Developing Innovative Translational Research Programs in Clinically Relevant Neurological Disorders.

AUTHOR CONTRIBUTIONS

L.E. conceived the project; L.E. and M.K. designed the experiments; M.K., A.L.F., and L.E. performed the experiments and collected the data; M.K. and L.E. analyzed and interpreted the data; M.K. and L.E. drafted and edited the manuscript.

FIGURE LEGENDS

Figure 1: Aging triggers the progressive development of excessive higher-order dendritic branching in PVD neurons.

(A) Schematic diagram of PVD neuron in control (CT) animals [*F49H12,4::GFP (wdIs51)*]. Black boxes indicate regions imaged. **(B)** A 'menorah' structure with orders of dendritic branching indicated. **(C)** Representative images of anterior (Zone 1) and posterior (Zone 2) sections of PVD neuron at Day 1 (D1) and D9 of adulthood in CT animals. Blue boxes indicate zoomed in section for Zone 1, Red boxes indicate zoomed in section for Zone 2. Yellow arrowheads indicate PVD soma, and blue arrowheads indicate PVD axon. White arrowheads indicate 5º dendritic branches and red arrowheads indicate 6º branches. Scale bar = 20 µM. **(D-E)** Quantification of 5º *(D)* and 6º *(E)* branches during aging in CT animals. *n* >50 per group. **(F-G)** Quantification 5º *(F)* and 6º *(G)* branches in CT animals at 15 ºC, 20 ºC, and 25 ºC. *n* >36/group. **(H-I)** Quantification of dorsal 6º branches normalized to the number of dorsal menorah *(H)* and ventral 6º branches normalized to the number of ventral menorah *(I)*. *n* >10/group. **(J-K)** Quantification of dorsal 6º branches normalized to dorsal 4º branches *(J)* and ventral 6º branches normalized to ventral 4º branches *(K)*. *n* >10/group. **(L-M)** Quantification of anterior 6º branches normalized to the number of anterior menorah *(L)* and posterior 6º branches normalized to the number of posterior menorah *(M)*. *n* >25/group. **(N-O)** Quantification of anterior 6º branches normalized to anterior 4º branches *(N)* and posterior 6º branches normalized to posterior 4º branches *(O)*. *n* >25/group. **(P)** Representative time-lapse images of actin dynamics in higher order branches during an 8-minute session at 2-minute intervals in D1 and D9 CT animals [*ser-2(3)p::GFP::UtrCH + ser-2(3)p::mCherry-PH(lxyEx51)*]. Yellow arrows indicate 2º and 3º branches. White arrowheads indicate 5º branches and red arrowheads indicate 6º branches, with asterisks indicating branches where a dynamic actin remodeling event occurs. Scale bar = 10 µm. **(Q-R)** Changes in the length of higher-order branches relative to their initial lengths were tracked using time-lapse imaging data obtained from D1*(Q)* and D9 *(R)* CT animals as in *(P)*. Measurements were taken for 5º and 6º dendrites branching from 4º and 5º dendrites, respectively, with each line representing a single higher-order branch. *n* (animals imaged) = 3/group. **(S)** Absolute change in branch length over 8 minutes in D1 and D9 CT animals, with each point representing a higher-order branch. *n* (animals to imaged) = 3/group. * $p<0.05$, ** $p<0.005$, *** $p<0.001$, **** $p<0.0001$.

Figure 2: Aging-associated excessive dendritic branching in PVD neurons correlates with proprioceptive deficits

(A) Representative images of movement tracks of control (CT) animal at D3 and D9 of adulthood. Scale bar = 50 µM. **(B-C)** Mean amplitude *(B)* and mean wavelength *(C)* measured from 100 tracks per animal in CT animals. Normalized for animal body length. *n* >28 per group. **(D-E)** Variability in amplitude *(D)* and wavelength *(E)* measured via coefficient of variability (CV) from 100 tracks per animal in CT animals. *n* >28/ group. **(F-I)** Correlation between proprioception measurements and number of PVD dorsal 6º dendritic branches. *n* >28/group. * $p<0.05$, *** $p<0.001$, **** $p<0.0001$.

Figure 3: Loss of skin collagen leads to early-onset of aging-associated excessive branching and proprioceptive deficit.

(A) Domain structures of COL-120 and DPY-5, with key features annotated. Adapted from CeCoIDB [118]. **(B-C)** Representative images of excessive PVD dendritic branching in *dpy-5* mutant [*dpy-5(e907); F49H12,4::GFP(wdIs51)*] *(B)* and *col-120* mutant (*col-120(sy1526); F49H12,4::GFP (wdIs51)*) *(C)* at D3 of adulthood. White arrowheads indicate 5º dendrites, and red arrowheads indicate 6º dendrites. Scale bar = 50 μM. **(D-E)** Quantification of 5º *(D)* and 6º *(E)* dendrites in CT, *dpy-5(e907)* mutant, and *dpy-5* rescue line 1 (epidermis-specific rescue driven by *dpy-7* promoter) animals. *n* >60 per group. **(F-G)** Quantification of 5º *(F)* and 6º *(G)* dendrites in CT, *col-120(sy1526)* mutant, and *col-120* rescue line 1 (epidermis-specific rescue driven by *dpy-7* promoter and *col-19* promoter) animals. *n* >55/group. **(H-I)** Quantification of 5º *(H)* and 6º *(I)* dendrites in empty vector (EV) and *dpy-5* RNAi treated animals. *n* >70/group. **(J-K)** Quantification of 5º *(J)* and 6º *(K)* dendrites in EV and *col-120* RNAi treated animals. *n* >70/group. **(L)** Representative images of movement tracks of D3 CT, D9 CT and D3 *col-120(sy1526)* mutant animals. Scale bar = 50 μM. **(M-N)** Mean wavelength *(M)* and mean amplitude *(N)* measured from 100 tracks per animal for D3 CT, D9 CT, and D3 *col-120(sy1526)* mutant animals. Normalized for animal body length. *n* >28/group. * $p<0.05$, ** $p<0.005$, *** $p<0.001$, **** $p<0.0001$.

<u>Figure 4: Overexpression of skin collagen mitigates aging-associated excessive dendritic branching in PVD neurons.</u>

(A-B) Quantification of 5º *(A)* and 6º *(B)* dendrites in control (CT) and *dpy-5* overexpression (epidermis-specific overexpression driven by *col-19* promoter) animals at D9 of adulthood. *n* >46 per group. **(C-D)** Quantification of 5º *(C)* and 6º *(D)* dendrites in CT and *col-120* overexpression (ubiquitous overexpression driven by *dpy-30* promoter) animals. *n* >63 per group. **(E)** Lifespan analysis of CT, *dpy-5* overexpression and *col-120* overexpression animals. No statistical significance was detected compared to CT. *n* >12 for each group. * $p<0.05$, ** $p<0.005$, *** $p<0.001$.

<u>Figure 5: Selective impact of skin collagens on the aging process of sensory neurons</u>

(A) Quantification of PVD dendritic beading in control (CT), *dpy-5(e907)* mutant, and *col-120(sy1526)* mutant animals at D3 of adulthood. Scored based on severity of beading phenotype. *n*>26 per group. **(B)** Schematic diagram of ALM and PLM neuron, with a representative image of the ALM neuron in CT [*mec-4p::GFP(zdIs5)*] and *dpy-5* mutant [*dpy-5(e907); mec-4p::GFP (zdIs51)*] animals at D3 of adulthood. Scale bar = 50 μM. White arrowhead indicates ectopic branching from ALM anterior neurite; yellow arrowheads indicate ALM soma. **(C-D)** Quantification of ectopic branches in ALM *(C)* and PLM neuron *(D)* in CT and *dpy-5(e907)* mutant animals at D3. Number of ectopic branches observed per animal is indicated. *n* >78 per group. **** $p<0.0001$.

<u>Figure 6: RIG-3/IgSF functions along with skin collagens to regulate aging-associated excessive PVD dendritic branching.</u>

(A-B) Quantification of 5º*(A)* and 6º *(B)* dendrites in empty vector (EV) and *rig-3* RNAi treated control animals (*F49H12,4::GFP (wdIs51)*) . *n*>84/group. **(C-D)** Quantification of 5º *(C)* and 6º *(D)* dendrites in control (CT, *ser-2(3)p::GFP (lxyEx77)*, see Methods) and *rig-3* mutant [*rig-3(ok2156); ser-2(3)p::GFP (lxyEx77)*] animals. *n* >86/group. **(E)** Quantification of 5º dendrites in *dpy-5(e907)* mutant animals treated with EV or *rig-3* RNAi, and in *col-120(sy1526)* mutant animals treated with EV or *rig-3* RNAi. *n* >84/group. **(F)** Quantification of 6º dendrites in *dpy-5(e907)* mutant animals treated with EV or

rig-3 RNAi, and in *col-120* mutant*(sy1526)* animals treated with EV or *rig-3* RNAi. *n* >84/group. * *p*<0.05, *** *p*<0.001, **** *p*<0.0001.

SUPPLEMENTAL FIGURE LEGENDS

Figure S1: Characterization of the aging PVD neuron

(A) Schematic diagram of the PVD neuron in control (CT) animals. The black box indicates the zone presented in the representative image of CT animals at Day 11 of adulthood. Yellow arrowheads indicate neuritic beads. Scale bar = 50 μM. **(B)** Correlation between PVD beading severity and harsh touch response in CT [*mec-4(u253)*; *F49H12,4::GFP(wdIs51)*] animals at D7. See Methods for scoring criteria. *n*>20 . **(C-F)** Quantification of the number of Dorsal 5º branches *(C)*, Ventral 5º branches *(D)*, Dorsal 6º branches *(E)*, and Ventral 6º branches *(F)* in CT [*F49H12,4::GFP(wdIs51)*] animals, *n* >54/group. **(G-J)** Quantification of number of Dorsal *(G)*, Ventral *(H)*, Anterior *(I)*, and Posterior *(J)* menorah. *n* >10/group. **(K-N)** Quantification of number of Dorsal *(K)*, Ventral *(L)*, Anterior *(M)*, and Posterior *(N)* 4º branches. *n* >10/group. **(O-R)** Quantification of number of Dorsal *(O)*, Ventral *(P)*, Anterior *(Q)*, and Posterior *(R)* 5º branches normalized to number of menorah. *n* >10/group. **(S-V)** Quantification of number of Dorsal *(S)*, Ventral *(T)*, Anterior *(U)*, and Posterior *(V)* 5º branches normalized to number of 4º branches. *n* >10/group. **(W-X)** Quantification of number of 5º *(W)* and 6º *(X)* branches normalized to body length. *n* >28 per group. * *p*<0.05, ** *p*<0.005, *** *p*<0.001, **** *p*<0.0001.

Figure S2: Actin and microtubule dynamics in the PVD neuron

(A) Split channel representative time-lapse images of actin dynamics in higher order branches during an 8 minute session at 2 minute intervals at Days 1 and 9 of adulthood in control animals [*ser-2(3)p::GFP::UtrCH + ser-2(3)p::mCherry-PH(lxyEx51)*]. Red channel displays the PVD neuron, while the green channel displays the actin in the PVD. **(B)** Split channel and merged images of microtubule localization in the PVD neuron at Day 7 in control animals [*ser-2(3)p::EMTB::GFP + ser-2(3)p::mCherry-PH(lxyEx48)*]. Red channel displays the PVD neuron, while the green channel displays the microtubules in the PVD.

Figure S3: Aging-associated dendritic branching correlated with proprioceptive deficits and neuritic beading

(A) Correlation between number of higher-order branches (5º and 6º) and harsh touch response in *mec-4* mutant (*mec-5(u253)*) animals at Day 7 of adulthood. Harsh touch response was scored based on the distance moved with a cumulative score ranging from 0 to 10, indicating impaired to normal response respectively. **(B-C)** Correlation between variability in amplitude (CV) and higher-order branches in control (CT) animals at Days 3 and 9 of adulthood. Higher-order branches are 5º branches *(B)* and 6º branches *(C)*. *n* >28 for each group. **(D-E)** Correlation between Wavelength CV and higher-order branches in CT animals at Days 3 and 9. Higher-order branches are 5º branches *(D)* and 6º branches *(E)*. *n* >28 for each group. **(F-G)** Correlation between Mean amplitude and higher-order branches in CT animals at Days 3 and 9. Higher-order branches are 5º branches *(F)* and 6º branches *(G)*. *n* >28 for each

group. **(H-I)** Correlation between Mean wavelength and higher-order branches in CT animals at Days 3 and 9. Higher-order branches are 5º branches *(H)* and 6º branches *(I)*. *n* >28 for each group. **(J-U)** Either dorsal or ventral branches were measured for individual animals. Only animals whose dorsal branches were measured were used for analysis of dorsal branch correlation, and the same for ventral branch analysis. **(J-M)** Correlation between proprioception measurements and number of ventral 6º branches at Days 3 and 9 in CT animals. Proprioceptive measurements are Amplitude CV *(J)*, Wavelength CV *(K)*, mean amplitude *(L)*, and mean wavelength *(M)*. *n* >28/group. **(N- Q)** Correlation between proprioception measurements and number of dorsal 5º branches at Days 3 and 9 in CT animals. Proprioceptive measurements are Amplitude CV *(N)*, Wavelength CV *(O)*, mean amplitude *(P)*, and mean wavelength *(Q)*. *n* >28/group. **(R- U)** Correlation between proprioception measurements and number of ventral 5º branches at Days 3 and 9 in CT animals. Proprioceptive measurements are Amplitude CV *(R)*, Wavelength CV *(S)*, mean amplitude *(T)*, and mean wavelength *(U)*. *n* >28/group. **(V-W)** Correlation between higher-order branching and the extent of neuritic beading in CT animals at Days 8 and 9 of adulthood. Higher-order branches are 5º branches *(V)* and 6º branches *(W)*. Beading severity is measured as 0- normal ,1- mild, 2- moderate, and 3 -severe. *n* >11/group.

Figure S4: Characterization of loss of skin collagens

(A) (Left) Volcano plot depicting changes in expression of skin collagens in D10 animals relative to L4 animals from the GSE176088 dataset. *col-120, dpy-5,* and *dpy-10* are shown in orange. (Right) qPCR verification of *dpy-5* and *col-120* mRNA expression levels in control (CT) animals at D1 and D7 of adulthood, represented as relative quantity, with *ama-1* as the housekeeping gene. **(B)** *dpy-5* and *col-120* mRNA expression levels after RNAi treatment relative to empty vector (EV) control represented as relative quantity z-score, with *ama-1* as the housekeeping gene. **(C)** Comparison of body lengths between control (CT) and *col-120* mutant animals at Day 3 of adulthood. *n* >25 per group. **(D)** Lifespan analysis of CT, *dpy-5* mutant and *col-120* mutant animals. *n* >16/group. **(E-F)** Quantification of 5º *(E)* and 6º *(F)* branches in CT, *dpy-5* mutant, and *dpy-5* rescue line 2 (Epidermis-specific rescue driven by *dpy7(SI)* promoter) animals at Day 3. *n* >20/group. **(G-H)** Quantification of 5º *(G)* and 6º *(H)* branches in CT, *col-120* mutant, and *col-120* rescue line 2 (Epidermis-specific rescue driven by *col19* promoter) animals at Day 3. *n* >81/group. **(I-J)** Quantification of 5º *(I)* and 6º *(J)* branches in CT, *dpy-5* mutant, and *col-120* mutant animals at L4 stage. *n* >20/group. **(K-L)** Quantification of 5º *(K)* and 6º *(L)* branches in empty vector (EV) animals at Day 3 and Day 9. *n*> 30/group. **(M-N)** Quantification of 5º *(M)* and 6º *(N)* branches in EV and *dpy-5* RNAi clone 2 at Day 3 of adulthood. *n* >23/group. **(O-P)** Quantification of 5º *(O)* and 6º *(P)* branches EV and *col-120* RNAi clone 2 at Day 3 of adulthood. *n* >30/group. **(Q-R)** Quantification of Wavelength CV *(Q)* and Amplitude CV *(R)* in CT Day 3, CT Day 9, and *col-120* mutant animals at Day 3 of adulthood. *n* >25/group. * $p<0.05$, ** $p<0.005$, *** $p<0.001$, **** $p<0.0001$.

Figure S5: Overexpression of skin collagens does not delay onset of proprioceptive deficit

(A-B) Quantification of 5º *(A)* and 6º *(B)* branches in control (CT) and *col-120* overexpression line 2 (Whole-tissue overexpression driven by *dpy30* promoter) animals at Day 9 of adulthood. *n* >20 for each group. **(B)** Additional replicate of lifespan analysis of CT, and *col-120* overexpression animals. n > 23/group. **(D-G)** Quantification of Mean wavelength normalized to control *(C)*, Mean amplitude

normalized to control *(D)*, Wavelength CV *(E)*, and Amplitude CV *(F)* in CT and *dpy-5* overexpression (Epidermis-specific overexpression driven by *col-19* promoter) animals. *n* >21/ group. ** *p*<0.005.

Figure S6: Additional mediators of excessive dendritic branching

(**A-B)** Quantification of 5º *(A)* and 6º *(B)* branches in empty vector (EV), *ina-1* RNAi, *ddr-2* RNAi, *sdn-1* RNAi treatment at Day 3 of adulthood. *n* >30 per group. **(C-D)** Quantification of 5º *(C)* and 6º *(D)* branches in control (CT, *F49H12,4::GFP(wdIs51)*) and *dpy-10* mutant (*dpy-10(e128); F49H12,4::GFP(wdIs51)*) animals. *n* = 50/group. **(E)** KEGG pathway analysis between control and *dpy-10* mutant animals. ** *p*<0.005,**** *p*<0.0001.

Table S1: Comparison of branching in PVDL and PVDR neurons

Difference between medians for WT animals at Day 3, 6, 9 for Right and Left PVD neurons' 5º and 6º branches. *n* >19 per group.

Table S2: Comparison of branching on dorsal-ventral side of PVD neuron

Difference between means/medians for control (CT) and experimental groups between Dorsal and Ventral sections of PVD neurons' 5º and 6º branches. Experimental groups are *dpy-5* mutant, *col-120* mutant, *dpy-5* overexpression, *col-120* overexpression, *dpy-5* RNAi, and *col-120* RNAi. *n* >19 per group.

METHODS

C. elegans Strains and Maintenance

C. elegans strains were maintained at 20 ºC, or as otherwise indicated, on Nematode Growth Medium (NGM) plates seeded with *E. coli* OP50 as described previously [119]. Only hermaphrodites were utilized for data generating experiments. Males were utilized for genetic crosses alone. For aging-related experiments, plates containing gravid hermaphrodites were bleached to produce age-synchronous progeny and to eliminate potential pathogenic microbes. Once the animals reached mid-L4 or late-L4 stage, they were transferred to NGM plates containing 100 µM 5' fluorodeoxyuridine (FUDR) (VWR, 76345-984) to prevent egg hatching and to maintain age-synchronous population [120,121]. Day 1 of adulthood was defined as occurring 24 hours after the L4 stage. For strain information, see Table S3.

DNA Constructs and Generation of Transgenes

Gateway cloning technology (ThermoFisher, K250020, 11791020) was used to create all DNA expression constructs, and information about the individual constructs is listed in Table S4. Primers were acquired from Millipore and ThermoFisher, and details are included in Table S3. The transgenic animals were generated using the standard procedures through microinjection [122]. In general, plasmid DNAs of interest were used at 10-100 ng/µL with the co-injection marker *ttx-3p::RFP* or *ttx-3p::GFP* at 50 ng/µL (see Tables S3 and S4). At least two independent transgenic lines were analyzed for each construct.

Fluorescent Microscopy

Fluorescent reporters were used to visualize and evaluate the morphology of ALM, PLM, and PVD neurons. Neuron morphology was phenotyped with a Zeiss Axio Imager M2 using 0.5 to 1% M9 dilution of 1-phenoxy-2-propanol (Fisher, P011825ML) to immobilize the animals. Representative images were collected with a Leica SP8 upright confocal microscope, using polystyrene beads (Polysciences, 00876-15, 0.1 µM diameter) to immobilize the animals [123]. Confocal images shown are projections of Z-stack images (0.5-1µm/slice) collected using 63X objective.

Quantification of Neuron Morphological Defects

wdIs51 (F49H12.4::GFP) [33] and *zdIs5 (mec-4p::GFP)* [124] were used to visualize PVD and ALM/PLM neurons, respectively. PVD excessive dendritic branching was assessed by quantifying the number of 5º and 6º branches. 5º branches were identified based on the established dendritic structure of the PVD, with 1º branches emerging from the soma, 2º branches emerging from the 1º, and 3º and 4º following the same pattern and forming 'menorah' units. 5º and 6º branches also follow this pattern and are observed within these 'menorah' (Fig. 1B). The number of 5º and 6º branches for each animal were counted for either the right or left PVD neuron for either the dorsal or ventral side, depending on which was clearly visible during the imaging session. For the assessment of the PVD dendritic beading phenotype, we quantified the number of bead- or bubble-like structures present along the dendrites of either PVDL or PVDR across the entire dendritic tree for each animal. An animal was considered as having the degenerative phenotype only if a total of ten or more bead- or bubble-like structures were observed in over five PVD menorahs [23]. For severity quantification in Figure 5A, an animal with 0-10 beading structures was scored as normal, 10-20 mild, 20-50 moderate, and >50 was scored as severe. In Figure S1B, a more detailed scoring system was employed: a score of 1 indicated 0-10 structures; 2 indicated 10-20; 3 indicated 20-30; 4 indicated 30-50; 5 indicated 50-100; 6 indicated 100-200; and 7 indicated more than 200 structures, or a number beyond countable. For ALM/PLM neurons, the number of ectopic branches sprouting from their main neurites were counted. For each experimental group, a

minimum of three independent replicates of 30 animals were always quantified alongside a control group in parallel to mitigate inherent variability. Experimenters scoring and analyzing assays were also blinded to the grouping information to reduce bias. *ser-2(3)p::GFP (lxyEx77)* was constructed to visualize PVD neurons when examining *rig-3* mutant animals, due to the difficulty in crossing *rig-3(ok2156)X* into *wdIs51 (F49H12.4::GFP)X*. The *ser-2(3)p::GFP (lxyEx77)* animals exhibited a larger body size than *wdIs51 (F49H12.4::GFP)*, likely due to different genetic backgrounds, which may explain the variation in branching numbers observed in the two PVD reporter strains at D3 of adulthood.

PVD Function Analysis: Harsh Touch Response

The measurement of the harsh touch response was conducted as previously described [23,32,125,126], with modifications to the scoring system. The PVD neurons in C. elegans are essential for mediating responses to harsh touch stimuli applied to the mid-body, typically triggering either forward or backward locomotion [31,32,126]. Since gentle touch activation of touch receptor neurons such as ALM, AVM, PLM, and PVM can induce similar behavioral reactions [32], to isolate the role of PVD neurons from the influence of other touch receptor neurons in our assays, we employed a *mec-4(u253)* mutant background with non-functional touch receptor neurons but intact PVD neuron functionality [85,127]. *mec-3(e1338)* mutants, which lack normal functioning in both PVD and other touch receptor neurons, were used as a positive control for 'no harsh touch response' [23,32,85]. Briefly, to measure the harsh touch response, a worm pick was used to gently prod the midsection of minimally moving. The elicited escape movement, either forward or reverse, was observed within 5 seconds following the touch. Scoring was based on the distance moved: a score of 1 was assigned if the animal moved more than one body length, a score of 0.5 if it moved between one-third and one body length, and a score of 0 if it did not move or moved less than one-third of a body length. Each animal underwent 10 trials, with intervals of 10-15 minutes between trials. The cumulative score from all trials ranged from 0, indicating severely impaired harsh touch response, to 10, denoting an optimal response.

PVD Function Analysis: Proprioception

Proprioceptive sensing specific to PVD neurons was assessed using a locomotion assay as described previously [64 30] with some modifications. On the day of assay, animals were transferred to fresh NGM plates seeded with OP50, one animal per plate, and allowed to roam freely for 2-3 hours at 20 ºC, until sufficient tracks were made in the bacterial lawn. The plate was then imaged using a digital camera attached to a Leica S9i stereomicroscope at 1X magnification. Three independent replicates of 10 animals each were assayed for each group. A total of 100 randomly selected wavelengths (distance between two adjacent peaks) and amplitudes (distance between peak and wavelength, perpendicular to wavelength) were measured using Fiji. All measurements were used in cases where animals had fewer than 100 measurements, with a minimum of 40 measurements per animal. All measurements were normalized to the body lengths of individual animals and units were converted to millimeters utilizing a reference slide. All animals subjected to proprioception assay were also examined under the Zeiss to quantify PVD dendritic branching.

Reverse Transcription-quantitative PCR

<u>TRI reagent method</u>

To quantify the change in expression level of collagens in aging, N2 WT animals at Day 1 and Day 7 of adulthood were collected. Animals were washed with M9 solution for three 30-minute washes, and total RNA was isolated with TRI reagent (Millipore Sigma, 93289-100mL).

10-worm lysis method

To test the efficiency of RNAi knockdown experiments, 10-worm lysis method [128] was used to prepare RNA samples from animals subjected to RNAi treatment. Briefly, 10 worms from each RNAi treatment group were collected and cleaned in H_2O before depositing in 1 µL of lysis buffer (0.25 mM EDTA (Merck), 5mM Tris pH 8.0 (Sigma-Aldrich), 0.5% Triton X-100, 0.5% Tween-20 1mg/mL proteinase K) [128]. The samples then underwent a lysis cycle via incubating in a thermal cycler for 15 minutes at 65 ºC followed by 1 minute at 85 ºC and storing at -80 ºC for at least 12 hours. Following this, 1.5 µL of additional lysis buffer was added to the original sample and incubated with the same lysis cycle. The lysed samples were then treated with dsDNAse (ThermoFisher, EN0771) by adding 0.5 µL each of 10X dsDNAse buffer and dsDNAse, 1.5 µL of ultrapure H_2O, and then incubating at 37 ºC for 15 minutes, 55 ºC for 5 minutes, and 65 ºC for 1 minute. The samples were then processed to reverse transcription.

Reverse transcription was performed with iScript Reverse Transcription Supermix for RT-qPCR (BioRad, 1708841). Quantitative real-time reverse transcription PCR was performed using TaqMan Gene Expression Assays (ThermoFisher, Ce02462726_m1, Ce02417736_s1, Ce02457574_g1) and iTaq Universal Probes Supermix (Bio-Rad, 1725131) to quantify the mRNA levels of *dpy-5* and *col-120,* and *ama-1* was used as a housekeeping control. Bio Rad CFX96 Touch Deep Well Real-time PCR Detection System was used to perform the qPCR and relative mRNA levels were calculated using comparative ΔΔCT method.

Lifespan Assay

Lifespan assay was performed using 30 animals per replicate for 3 independent replicates. L4 animals were transferred to 100 µM FUDR plates and scored daily. An animal was considered dead when it no longer responded to gentle prodding with a platinum wire and displayed a lack of pharyngeal pumping. Lifespan was calculated from the time animals were placed on the FUDR plates until they were scored as dead. Animals that died due to protruding/bursting vulva, internal hatching, as well as animals that crawled off the agar were censored.

PVD Time-lapse Imaging and Analysis

The PVD higher-order branches in young adults are highly dynamic structures [33]. Time-lapse imaging was performed utilizing the Leica SP8 upright confocal microscope, using polystyrene beads and 2% agarose pads to immobilize the animals [123]. Control animals (*ser2(3)p::mCherry-PH; ser2(3)p::GFP::UtrCH*) were imaged at Day 1 and Day 9 of adulthood. Each imaging session was 8 minutes long with 2-minute intervals, and the images are projections of Z-stack images collected using 63X objective using both the red and green channels. The branch dynamics were quantified using Fiji to measure the length of individual higher-order branches at every imaging time-point. An assessment of the actin dynamics was made by visually assessing the movement of the GFP-labelled actin in the higher-order branches.

Adulthood-specific RNAi

For RNAi experiments, NGM plates containing isopropylthiogalactoside (IPTG) (Millipore Sigma, I6758-5G) were utilized to ensure expression of the appropriate double-stranded RNA by the HT115 bacteria. FUDR at a concentration of 100 µM was externally added to these plates following growth of the HT115 bacterial lawn. For RNAi knockdown of genes of interest, CT animals (or mutant animals, as indicated in Results) at mid-L4 or late L4 stage were transferred onto RNAi plates seeded with HT115 bacteria expressing the appropriate dsRNA. The dendritic branching of the PVD neuron, and the

proprioception of the animals were assessed 72 hours later at Day 3 of adulthood. The RNAi clones were created using PCR from cDNA or obtained from the Vidal RNAi library (distributed by Horizon Discovery, Key Resources Table). Empty L4440 plasmid was utilized as a negative control. TJ356 *[zIs356 (daf-16p::daf-16a/b::GFP)]* animals with empty-vector or *daf-2* RNAi treatment were utilized as a positive control. If the RNAi treatment was successful, the *daf-2* RNAi treated animals would display nuclear translocation of DAF-16::GFP, if unsuccessful, the DAF-16::GFP would remain in the cytoplasm [129].

Gene expression datasets and pathway enrichment analyses

Publicly available gene expression datasets were obtained from the Gene Expression Omnibus [130,131]. To assess the expression changes of collagen genes during normal aging, we analyzed the RNA-seq transcriptomic dataset GSE176088 [69], which includes three samples from L4 N2/wild-type worms and three samples from Day 10 N2 worms, all maintained at 20°C, using the online tool GEO2R. To gain insights into the potential downstream mechanisms by which skin cuticular collagens influence neuronal integrity, we analyzed microarray profiling data (GSE19310) from N2 and *dpy-10(e128)* mutant worms at the young adult stage, using GEO2R to identify differentially expressed genes (DEGs). Genes with Log2-fold change ≥ 1.5 and a p-value < 0.05 were considered as DEGs. The biological functions of the downregulated genes in *dpy-10(e128)* mutant worms were further explored through Kyoto Encyclopedia of Genes and Genomes (KEGG) enrichment analysis [132] using the Database for Annotation, Visualization and Integrated Discovery (DAVID, version 2021) [133,134]. A false discovery rate (FDR) $<$ 0.01 was applied as the threshold for statistical significance. The top 10 significant KEGG pathways were visualized in a bubble graph, where the Rich factor represents the ratio of DEGs annotated within a specific pathway term to the total number of genes annotated in that pathway.

Statistical Analysis

All data processing, statistical analyses, and graph plotting were performed with GraphPad Prism software. Prior to statistical testing, the normality of datasets was assessed using the D'Agostino & Pearson test. For comparisons between an experimental and a control group, we used an unpaired t-test with Welch's correction for normally distributed data, and the Mann-Whitney test for non-normally distributed data. When comparing three or more groups, either one-way ANOVA or the Kruskal-Wallis test (non-parametric, followed by Dunn's multiple comparisons post-hoc analysis. Pearson's correlation test was applied for correlation analyses. Log-Rank test was used to analyze lifespan data. Bar graphs display the mean ± SEM for normally distributed data, and the median with interquartile range for non-normally distributed data.

Table S3

Strain	Genotype	Notes
N2	Wild type	CGC
NC1686	*F49H12.4::GFP;unc-119(+)(wdIs51)X*	CGC, Used to create ELZ55
BC10008	*dpy-5(e907) I; sEx10008*	CGC, Used to create ELZ23
CB128	*dpy-10(e128) II;*	CGC, Used to create ELZ43
CZ10175	*zdIs5 [mec-4p::GFP + lin-15(+)] I*	CGC
PS8819	*col-120(sy1526)IV*	CGC, Used to create ELZ60
RB1712	*rig-3(ok2156) X*	CGC, Used to create ELZ155
TJ356	*zIs356 [daf-16p::DAF-16a/b::GFP; rol-6] IV*	CGC

ELZ23	*F49H12,4::GFP;unc-119(+)(wdIs51)X; dpy-5(e907) I*	-
ELZ30	*zdIs5 [mec-4p::GFP + lin-15(+)] I; dpy-5(e907) I*	-
ELZ43	*dpy-10(e128) II; F49H12,4::GFP; unc-119(+)(wdIs51) X*	
ELZ55	*F49H12,4::GFP; unc-119(+)(wdIs51) X*	1x outcross of NC1686
ELZ60	*col-120(sy1526)IV; F49H12,4::GFP;unc-119(+)(wdIs51)X*	-
ELZ78	*F49H12.4::GFP;unc-119(+)(wdIs51)X; dpy-30p::col-120 cDNA(lxyEx16)*	100ng/μL PELZ32 + 50ng/μL PELZ5 into ELZ55
ELZ76	*F49H12,4::GFP;unc-119(+)(wdIs51)X; dpy-30p::col-120 cDNA(lxyEx14)*	100ng/μL PELZ32 + 50ng/μL PELZ5 into ELZ55
ELZ83	*col-120(sy1526)IV; F49H12.4::GFP;unc-119(+)(wdIs51)X; dpy-30p::col-120 cDNA(lxyEx21)*	10ng/μL PELZ32 + 50ngμL PELZ5 into ELZ60
ELZ86	*F49H12.4::GFP;unc-119(+)(wdIs51)X; col-19p::dpy-5 gDNA (lxyEx24)*	100 ng/μL PELZ19 into ELZ55
ELZ90	*col-120(sy1526)IV; F49H12,4::GFP;unc-119(+)(wdIs51)X; dpy7p::col120+ col-19p::col120(lxyEx26)*	20ng/μL PELZ31 + 20 ng/μL PELZ37 + 50 ng/μL PELZ5 into ELZ60
ELZ121	*ser-2(3)p::EMTB::GFP + ser-2(3)p::mCherry-PH(lxyEx48)*	4ng/μL PNYL931 + 4ng/μL PNYL720 + 50ng/μL PELZ5 to inN2
ELZ124	*ser-2(3)p::GFP::UtrCH + ser-2(3)p::mCherry-PH(lxyEx51)*	4 ng/μL PNYL930 + 6ng/μL PNYL720 + 50 ng/μL PELZ5 into N2
ELZ132	*F49H12,4::GFP;unc-119(+)(wdIs51)X; dpy-5(e907)I; dpy-7p::dpy5(lxyEx58)*	30 ng/μL PELZ75 + 50 ng/μL PELZ5 into ELZ23
ELZ133	*dpy-5 (e907)I; F49H12.4::GFP;unc-119(+)(wdIs51)X; dpy-7p::dpy-5 cDNA (lxyEx58)*	30 ng/μL PELZ75 + 50 ng/μL PELZ5 into ELZ23
ELZ150	*col-120(sy1526)IV; F49H12,4::GFP;unc-119(+)(wdIs51)X*	10 ng/μL PELZ37+ 50 ng/μL PELZ5 into ELZ60
ELZ155	*rig-3(ok2156) X*	4X outcross of RB1712
ELZ161	*ser-2(3)p::GFP (lxyEx77)*	10 ng/μL PELZ47+ 50 ng/μL PELZ4 into N2
ELZ166	*rig-3(ok2156)X; ser-2(3)p::GFP (lxyEx77)*	ELZ161 crossed with ELZ155

Table S4

Plasmid number	Plasmid description
PELZ4	*ttx-3p::GFP*
PCZGY2261	*ser2(3)p GTW*
PNYL720	*ser-2(3)p::mCherry-PH*
PNYL930	*ser-2(3)p::GFP-UtrCH*
PNYL931	*ser-2(3)p::EMTB::GFP*

PELZ5	*ttx-3p::RFP*
PELZ17	*ser2(3)p::mKate*
PELZ19	*col-19p::dpy-5 cDNA*
PELZ23	*L4440::dpy-5*
PELZ24	*dpy-7p::dpy-5*
PELZ25	*dpy-30p::dpy-5*
PELZ31	*dpy-7p::col-120*
PELZ32	*dpy-30p::col120 cDNA*
PELZ37	*col-19p::col-120 cDNA*
PELZ44	*col-120::L4440*
PELZ45	*col-120(1)::L4440*
PELZ46	*col-120(2)::L4440*
PELZ47	*ser-2(3)p::GFP*
PELZ48	*dpy-5::L4440*
PELZ49	*pat-2(1)::L4440*
PELZ50	*pat-2(2)::L4440*
PELZ51	Empty DEST backbone
PELZ59	*pat-2/col-120::L4440*
PELZ71	*dpy30p GTW (tbb-2 3'UTR)*
PELZ72	*dpy-30p (tbb-2 3'UTR)::col-120*
PELZ73	*dpy-30p (tbb-2 3'UTR)::dpy-5*
PELZ74	*dpy-7p GTW (unc-54 3'UTR)*
PELZ75	*dpy-7p (unc-54 3'UTR)::dpy-5*
PELZ76	*dpy-7p (unc-54 3'UTR)::col-120*
C. elegans RNAi feeding library, Horizon Discovery	*L4440::rig-3*
C. elegans RNAi feeding library, Horizon Discovery	*L4440::ina-1*
C. elegans RNAi feeding library, Horizon Discovery	*L4440::ddr-2*
C. elegans RNAi feeding library, Horizon Discovery	*L4440::sdn-1*

Table S5

Primer name	Primer sequence (5'-3')	Purpose
ok2156 Forward 1.4	CGTCATTTCATCAGAAGCCATG	Forward genotyping primer for rig-3(*ok2156*)
ok2156 Reverse 1.2	CCTGTAATAGAGTCGTTTACAACTTG TTTC	Reverse genotyping primer for rig-3(*ok2156*)
ok2156 Reverse 2	GTCATCTGAATCATTGGTTCTTTAC	Reverse genotyping primer for rig-3(*ok2156*)
Pdpy-7-SI-BB-F	ACTAGTGGATCCCCCGGGC	Forward primer for *dpy-7p* Gibson assembly backbone
Pdpy-7-SI-BB-R2	TTATCTGGAACAAAATGTAAGAATA TTCTTAAAAATTG	Reverse primer for *dpy-7p* Gibson Assembly backbone
Pdpy-7-SI-F2	CAATTTTTAAGAATATTCTTACATTT TGTTCCAGATAAACATACCGGGATT GGCCAAAG	Forward primer for *dpy-7p* Gibson Assembly

Pdpy-7-SI-R	GCCCGGGGGATCCACTAGTTTTTTCTACCGGTACCCTCC	Reverse primer for *dpy-7p* Gibson Assembly
Pdpy-30-SI-BB-F2	AAGCTTGATATCACAAGTTTGTACAAAAAAGCTG	Forward primer for *dpy-30p* Gibson Assembly backbone
Pdpy-30-SI-BB-R2	CTTGGTTTTTGCTCGATTTCTGAAAC	Reverse primer for *dpy-30p* Gibson Assembly backbone
Pdpy-30-SI-F2	GTTTCAGAAATCGAGCAAAAACCAAGACATACCGGGATTGGCCAAAG	Forward primer for *dpy-30p* Gibson Assembly
Pdpy-30-SI-R2	CAGCTTTTTTGTACAAACTTGTGATATCAAGCTTTTTTTCTACCGGTACCCTCC	Reverse primer for *dpy-30p* Gibson Assembly
Dpy-5-For	TTA GAC GCG TCT GCG CTT TCT CTC TG	Forward primer for *dpy-5* cDNA amplification
Dpy-5-Rev	ATGGTAAAGGCCGTCGTCGGATTCG	Reverse primer for *dpy-5* cDNA amplification
dpy-5(e907)-F1	GAAGCATGGGTCTCGTTAG	Forward genotyping primer for *dpy-5*
dpy-5(e907)-F2	GTCCTGGAGTTCCTTGATC	Forward genotyping primer for *dpy-5*
dpy-5(e907)-R	GAAGGTGTGTCCTCATGG	Reverse genotyping primer for *dpy-5*
Col-120 For	ATGAATTTGAAGAAGAATTTAGTGAATTCTGAAGAGGATG	Forward primer for *col-120* cDNA amplification
Col-120 Rev	TTAGTATCCAGGAGCAGTTCGTGGAGGTG	Reverse primer for *col-120* cDNA amplification
Col-120(sy2156)-F	GTTGCTTTCGTGGCGACTG	Forward genotyping primer for *col-120*
Col-120(sy2156)-R	CCTCCATATCCAGCTTGTC	Reverse genotyping primer for *col-120*
rig-3 For	ATGGGACGACTACTTGCCAAGATG	Forward primer for *rig-3* cDNA amplification
rig-3 Rev	TTAGATAAAAAGACAGACAAAAAATAACGTG	Reverse primer for *rig-3* cDNA amplification
newdpy5 For	GCAGGCTCCGAATTCGCCCTTAACCCAGGAGCCCCAGGAG	Forward primer for *dpy-5::L4440* site-directed mutagenesis
newdpy5 Rev	CTCCTGGGGCTCCTGGGTTAAGGGCGAATTCGGAGCCTGC	Reverse primer for *dpy-5::L4440* site-directed mutagenesis
newcol120 For 1	CCAGTAAAAAGACAAGCTGGATGGGCGAATTCGACCCAGCTTTCTTGTAC	Forward primer for *col-120(1)::L4440* site-directed mutagenesis
newcol120 Rev 1	GTACAAGAAAGCTGGGTCGAATTCGCCCATCCAGCTTGTCTTTTTACTGG	Reverse primer for *col-120(1)::L4440* site-directed mutagenesis

newcol120 For 2	GCAGGCTCCGAATTCGCCCTTTCTTCTTCCGATTCTTGTTG	Forward primer for *col-120(2)::L4440* site-directed mutagenesis
newcol120 Rev 2	CAACAAGAATCGGAAGAAGAAAGGGCGAATTCGGAGCCTGC	Reverse primer for *col-120(2)::L4440* site-directed mutagenesis

REFERENCES

1 Bouche, P. Neuropathy of the elderly. *Rev Neurol (Paris)* **176**, 733-738, doi:10.1016/j.neurol.2019.11.007 (2020).

2 Hicks, C. W., Wang, D., Windham, B. G., Matsushita, K. & Selvin, E. Prevalence of peripheral neuropathy defined by monofilament insensitivity in middle-aged and older adults in two US cohorts. *Sci Rep* **11**, 19159, doi:10.1038/s41598-021-98565-w (2021).

3 Martyn, C. N. & Hughes, R. A. Epidemiology of peripheral neuropathy. *J Neurol Neurosurg Psychiatry* **62**, 310-318, doi:10.1136/jnnp.62.4.310 (1997).

4 Verghese, J., Bieri, P. L., Gellido, C., Schaumburg, H. H. & Herskovitz, S. Peripheral neuropathy in young-old and old-old patients. *Muscle Nerve* **24**, 1476-1481, doi:10.1002/mus.1171 (2001).

5 Watson, J. C. & Dyck, P. J. Peripheral Neuropathy: A Practical Approach to Diagnosis and Symptom Management. *Mayo Clin Proc* **90**, 940-951, doi:10.1016/j.mayocp.2015.05.004 (2015).

6 Castelli, G., Desai, K. M. & Cantone, R. E. Peripheral Neuropathy: Evaluation and Differential Diagnosis. *Am Fam Physician* **102**, 732-739 (2020).

7 Li, X. *et al.* Proteins secreted by brain arteriolar smooth muscle cells are instructive for neural development. *Mol Brain* **15**, 97, doi:10.1186/s13041-022-00983-y (2022).

8 Goodness, T. P., Albers, K. M., Davis, F. E. & Davis, B. M. Overexpression of nerve growth factor in skin increases sensory neuron size and modulates Trk receptor expression. *Eur J Neurosci* **9**, 1574-1585, doi:10.1111/j.1460-9568.1997.tb01515.x (1997).

9 Krimm, R. F., Davis, B. M., Noel, T. & Albers, K. M. Overexpression of neurotrophin 4 in skin enhances myelinated sensory endings but does not influence sensory neuron number. *J Comp Neurol* **498**, 455-465, doi:10.1002/cne.21074 (2006).

10 Albers, K. M. & Davis, B. M. The skin as a neurotrophic organ. *Neuroscientist* **13**, 371-382, doi:10.1177/1073858407013004090 1 (2007).

11 Dong, X., Liu, O. W., Howell, A. S. & Shen, K. An extracellular adhesion molecule complex patterns dendritic branching and morphogenesis. *Cell* **155**, 296-307, doi:10.1016/j.cell.2013.08.059 (2013).

12 Ziegenfuss, J. S. & Grueber, W. B. SAX-7 and menorin light the path for dendrite morphogenesis. *Cell* **155**, 269-271, doi:10.1016/j.cell.2013.09.029 (2013).

13 Yang, W. K. & Chien, C. T. Beyond being innervated: the epidermis actively shapes sensory dendritic patterning. *Open Biol* **9**, 180257, doi:10.1098/rsob.180257 (2019).
14 Salzberg, Y. *et al.* Skin-derived cues control arborization of sensory dendrites in Caenorhabditis elegans. *Cell* **155**, 308-320, doi:10.1016/j.cell.2013.08.058 (2013).
15 Jiang, N. *et al.* A conserved morphogenetic mechanism for epidermal ensheathment of nociceptive sensory neurites. *Elife* **8**, doi:10.7554/eLife.42455 (2019).
16 Verdú, E., Ceballos, D., Vilches, J. J. & Navarro, X. Influence of aging on peripheral nerve function and regeneration. *J Peripher Nerv Syst* **5**, 191-208, doi:10.1046/j.1529-8027.2000.00026.x (2000).
17 Valdez, G. Effects of disease-afflicted and aging neurons on the musculoskeletal system. *Bone* **122**, 31-37, doi:10.1016/j.bone.2019.01.023 (2019).
18 Hunter, S. K., Pereira, H. M. & Keenan, K. G. The aging neuromuscular system and motor performance. *J Appl Physiol (1985)* **121**, 982-995, doi:10.1152/japplphysiol.00475.2016 (2016).
19 Correia, C. *et al.* Global Sensory Impairment in Older Adults in the United States. *J Am Geriatr Soc* **64**, 306-313, doi:10.1111/jgs.13955 (2016).
20 Takeuchi, H. *et al.* Neuritic beading induced by activated microglia is an early feature of neuronal dysfunction toward neuronal death by inhibition of mitochondrial respiration and axonal transport. *J Biol Chem* **280**, 10444-10454, doi:10.1074/jbc.M413863200 (2005).
21 Tan, Z. *et al.* Mutant ubiquitin found in Alzheimer's disease causes neuritic beading of mitochondria in association with neuronal degeneration. *Cell Death Differ* **14**, 1721-1732, doi:10.1038/sj.cdd.4402180 (2007).
22 Suzumura, A. [Neurotoxicity by microglia: the mechanisms and potential therapeutic strategy]. *Fukuoka Igaku Zasshi* **100**, 243-247 (2009).
23 E, L. *et al.* An Antimicrobial Peptide and Its Neuronal Receptor Regulate Dendrite Degeneration in Aging and Infection. *Neuron* **97**, 125-138.e125, doi:10.1016/j.neuron.2017.12.001 (2018).
24 Lauria, G. *et al.* Epidermal innervation: changes with aging, topographic location, and in sensory neuropathy. *J Neurol Sci* **164**, 172-178, doi:10.1016/s0022-510x(99)00063-5 (1999).
25 Thomas, S. *et al.* Abnormal intraepidermal nerve fiber density in disease: A scoping review. *Front Neurol* **14**, 1161077, doi:10.3389/fneur.2023.1161077 (2023).
26 Rosenheimer, J. L. & Smith, D. O. Differential changes in the end-plate architecture of functionally diverse muscles during aging. *J Neurophysiol* **53**, 1567-1581, doi:10.1152/jn.1985.53.6.1567 (1985).
27 Kravtsov, V., Oren-Suissa, M. & Podbilewicz, B. The fusogen AFF-1 can rejuvenate the regenerative potential of adult dendritic trees by self-fusion. *Development* **144**, 2364-2374, doi:10.1242/dev.150037 (2017).
28 Tsalik, E. L. *et al.* LIM homeobox gene-dependent expression of biogenic amine receptors in restricted regions of the C. elegans nervous system. *Dev Biol* **263**, 81-102, doi:10.1016/s0012-1606(03)00447-0 (2003).
29 Oren-Suissa, M., Hall, D. H., Treinin, M., Shemer, G. & Podbilewicz, B. The fusogen EFF-1 controls sculpting of mechanosensory dendrites. *Science* **328**, 1285-1288, doi:10.1126/science.1189095 (2010).
30 Tao, L. *et al.* Parallel Processing of Two Mechanosensory Modalities by a Single Neuron in C. elegans. *Dev Cell* **51**, 617-631.e613, doi:10.1016/j.devcel.2019.10.008 (2019).
31 Chatzigeorgiou, M. *et al.* Specific roles for DEG/ENaC and TRP channels in touch and thermosensation in C. elegans nociceptors. *Nat Neurosci* **13**, 861-868, doi:10.1038/nn.2581 (2010).

32 Way, J. C. & Chalfie, M. The mec-3 gene of Caenorhabditis elegans requires its own product for maintained expression and is expressed in three neuronal cell types. *Genes Dev* **3**, 1823-1833, doi:10.1101/gad.3.12a.1823 (1989).
33 Smith, C. J. *et al.* Time-lapse imaging and cell-specific expression profiling reveal dynamic branching and molecular determinants of a multi-dendritic nociceptor in C. elegans. *Dev Biol* **345**, 18-33, doi:10.1016/j.ydbio.2010.05.502 (2010).
34 White, J. G., Southgate, E., Thomson, J. N. & Brenner, S. The structure of the nervous system of the nematode Caenorhabditis elegans. *Philos Trans R Soc Lond B Biol Sci* **314**, 1-340, doi:10.1098/rstb.1986.0056 (1986).
35 Halevi, S. *et al.* The C. elegans ric-3 gene is required for maturation of nicotinic acetylcholine receptors. *EMBO J* **21**, 1012-1020, doi:10.1093/emboj/21.5.1012 (2002).
36 Saberi-Bosari, S., Flores, K. B. & San-Miguel, A. Deep learning-enabled analysis reveals distinct neuronal phenotypes induced by aging and cold-shock. *BMC Biol* **18**, 130, doi:10.1186/s12915-020-00861-w (2020).
37 Menzies, F. M., Fleming, A. & Rubinsztein, D. C. Compromised autophagy and neurodegenerative diseases. *Nat Rev Neurosci* **16**, 345-357, doi:10.1038/nrn3961 (2015).
38 Jin, M. *et al.* Soluble amyloid beta-protein dimers isolated from Alzheimer cortex directly induce Tau hyperphosphorylation and neuritic degeneration. *Proc Natl Acad Sci U S A* **108**, 5819-5824, doi:10.1073/pnas.1017033108 (2011).
39 Faerman, I. *et al.* Autonomic neuropathy in the skin: a histological study of the sympathetic nerve fibres in diabetic anhidrosis. *Diabetologia* **22**, 96-99, doi:10.1007/BF00254836 (1982).
40 Ashford, J. W., Soultanian, N. S., Zhang, S. X. & Geddes, J. W. Neuropil threads are collinear with MAP2 immunostaining in neuronal dendrites of Alzheimer brain. *J Neuropathol Exp Neurol* **57**, 972-978, doi:10.1097/00005072-199810000-00009 (1998).
41 Lauwers, E. *et al.* Neuropathology and neurodegeneration in rodent brain induced by lentiviral vector-mediated overexpression of alpha-synuclein. *Brain Pathol* **13**, 364-372, doi:10.1111/j.1750-3639.2003.tb00035.x (2003).
42 O'Donnell, K. C. *et al.* Axon degeneration and PGC-1alpha-mediated protection in a zebrafish model of alpha-synuclein toxicity. *Dis Model Mech* **7**, 571-582, doi:10.1242/dmm.013185 (2014).
43 Kenyon, C. J. The genetics of ageing. *Nature* **464**, 504-512, doi:10.1038/nature08980 (2010).
44 Vakkayil, K. L. & Hoppe, T. Temperature-Dependent Regulation of Proteostasis and Longevity. *Front Aging* **3**, 853588, doi:10.3389/fragi.2022.853588 (2022).
45 Chen, Y. L. *et al.* Adiponectin receptor PAQR-2 signaling senses low temperature to promote C. elegans longevity by regulating autophagy. *Nat Commun* **10**, 2602, doi:10.1038/s41467-019-10475-8 (2019).
46 Xiao, R. *et al.* A genetic program promotes C. elegans longevity at cold temperatures via a thermosensitive TRP channel. *Cell* **152**, 806-817, doi:10.1016/j.cell.2013.01.020 (2013).
47 Lee, S. J. & Kenyon, C. Regulation of the longevity response to temperature by thermosensory neurons in Caenorhabditis elegans. *Curr Biol* **19**, 715-722, doi:10.1016/j.cub.2009.03.041 (2009).
48 Klass, M. R. Aging in the nematode Caenorhabditis elegans: major biological and environmental factors influencing life span. *Mech Ageing Dev* **6**, 413-429, doi:10.1016/0047-6374(77)90043-4 (1977).

49 Kaech, S., Parmar, H., Roelandse, M., Bornmann, C. & Matus, A. Cytoskeletal microdifferentiation: a mechanism for organizing morphological plasticity in dendrites. *Proc Natl Acad Sci U S A* **98**, 7086-7092, doi:10.1073/pnas.111146798 (2001).
50 Stewart, A., Tsubouchi, A., Rolls, M. M., Tracey, W. D. & Sherwood, N. T. Katanin p60-like1 promotes microtubule growth and terminal dendrite stability in the larval class IV sensory neurons of Drosophila. *J Neurosci* **32**, 11631-11642, doi:10.1523/JNEUROSCI.0729-12.2012 (2012).
51 Burkel, B. M., von Dassow, G. & Bement, W. M. Versatile fluorescent probes for actin filaments based on the actin-binding domain of utrophin. *Cell Motil Cytoskeleton* **64**, 822-832, doi:10.1002/cm.20226 (2007).
52 Chia, P. H., Chen, B., Li, P., Rosen, M. K. & Shen, K. Local F-actin network links synapse formation and axon branching. *Cell* **156**, 208-220, doi:10.1016/j.cell.2013.12.009 (2014).
53 Richardson, C. E. *et al.* PTRN-1, a microtubule minus end-binding CAMSAP homolog, promotes microtubule function in Caenorhabditis elegans neurons. *Elife* **3**, e01498, doi:10.7554/eLife.01498 (2014).
54 Shaye, D. D. & Greenwald, I. The disease-associated formin INF2/EXC-6 organizes lumen and cell outgrowth during tubulogenesis by regulating F-actin and microtubule cytoskeletons. *Dev Cell* **32**, 743-755, doi:10.1016/j.devcel.2015.01.009 (2015).
55 Tang, L. T. *et al.* TIAM-1/GEF can shape somatosensory dendrites independently of its GEF activity by regulating F-actin localization. *Elife* **8**, doi:10.7554/eLife.38949 (2019).
56 Liu, X. *et al.* Atlastin-1 regulates morphology and function of endoplasmic reticulum in dendrites. *Nat Commun* **10**, 568, doi:10.1038/s41467-019-08478-6 (2019).
57 Raiders, S. *et al.* Engulfed by Glia: Glial Pruning in Development, Function, and Injury across Species. *J Neurosci* **41**, 823-833, doi:10.1523/JNEUROSCI.1660-20.2020 (2021).
58 Chiu, H. *et al.* Engulfing cells promote neuronal regeneration and remove neuronal debris through distinct biochemical functions of CED-1. *Nat Commun* **9**, 4842, doi:10.1038/s41467-018-07291-x (2018).
59 Nichols, A. L. A. *et al.* The Apoptotic Engulfment Machinery Regulates Axonal Degeneration in C. elegans Neurons. *Cell Rep* **14**, 1673-1683, doi:10.1016/j.celrep.2016.01.050 (2016).
60 Raiders, S. *et al.* Glia actively sculpt sensory neurons by controlled phagocytosis to tune animal behavior. *Elife* **10**, doi:10.7554/eLife.63532 (2021).
61 Liao, C. P., Li, H., Lee, H. H., Chien, C. T. & Pan, C. L. Cell-Autonomous Regulation of Dendrite Self-Avoidance by the Wnt Secretory Factor MIG-14/Wntless. *Neuron* **98**, 320-334 e326, doi:10.1016/j.neuron.2018.03.031 (2018).
62 Husson, S. J. *et al.* Optogenetic analysis of a nociceptor neuron and network reveals ion channels acting downstream of primary sensors. *Curr Biol* **22**, 743-752, doi:10.1016/j.cub.2012.02.066 (2012).
63 Albeg, A. *et al.* C. elegans multi-dendritic sensory neurons: morphology and function. *Mol Cell Neurosci* **46**, 308-317, doi:10.1016/j.mcn.2010.10.001 (2011).
64 Tavernarakis, N., Shreffler, W., Wang, S. & Driscoll, M. unc-8, a DEG/ENaC family member, encodes a subunit of a candidate mechanically gated channel that modulates C. elegans locomotion. *Neuron* **18**, 107-119, doi:10.1016/s0896-6273(01)80050-7 (1997).
65 Ko, S. U., Simonsick, E. M., Deshpande, N., Studenski, S. & Ferrucci, L. Ankle Proprioception-Associated Gait Patterns in Older Adults: Results from the Baltimore Longitudinal Study of Aging. *Med Sci Sports Exerc* **48**, 2190-2194, doi:10.1249/MSS.0000000000001017 (2016).

66 Wiesmeier, I. K., Dalin, D. & Maurer, C. Elderly Use Proprioception Rather than Visual and Vestibular Cues for Postural Motor Control. *Front Aging Neurosci* **7**, 97, doi:10.3389/fnagi.2015.00097 (2015).
67 Henry, M. & Baudry, S. Age-related changes in leg proprioception: implications for postural control. *J Neurophysiol* **122**, 525-538, doi:10.1152/jn.00067.2019 (2019).
68 Callisaya, M. L., Blizzard, L., Schmidt, M. D., McGinley, J. L. & Srikanth, V. K. Ageing and gait variability--a population-based study of older people. *Age Ageing* **39**, 191-197, doi:10.1093/ageing/afp250 (2010).
69 Yi, S. & Rui, X. (2021).
70 Stammers, M. *et al.* Age-related changes in the physical properties, cross-linking, and glycation of collagen from mouse tail tendon. *J Biol Chem* **295**, 10562-10571, doi:10.1074/jbc.RA119.011031 (2020).
71 Kehlet, S. N. *et al.* Age-related collagen turnover of the interstitial matrix and basement membrane: Implications of age- and sex-dependent remodeling of the extracellular matrix. *PLoS One* **13**, e0194458, doi:10.1371/journal.pone.0194458 (2018).
72 Varani, J. *et al.* Decreased collagen production in chronologically aged skin: roles of age-dependent alteration in fibroblast function and defective mechanical stimulation. *Am J Pathol* **168**, 1861-1868, doi:10.2353/ajpath.2006.051302 (2006).
73 Fatima, I. *et al.* Skin Aging in Long-Lived Naked Mole-Rats Is Accompanied by Increased Expression of Longevity-Associated and Tumor Suppressor Genes. *J Invest Dermatol* **142**, 2853-2863 e2854, doi:10.1016/j.jid.2022.04.028 (2022).
74 Chisholm, A. D. & Hsiao, T. I. The *C. elegans* epidermis as a model skin. I: development, patterning, and growth. *Wiley Interdiscip Rev Dev Biol.* (2013).
75 Kramer, J. M., Johnson, J. J., Edgar, R. S., Basch, C. & Roberts, S. The sqt-1 gene of C. elegans encodes a collagen critical for organismal morphogenesis. *Cell* **55**, 555-565, doi:10.1016/0092-8674(88)90214-0 (1988).
76 Chisholm, A. D. & Xu, S. The Caenorhabditis elegans epidermis as a model skin. II: differentiation and physiological roles. *Wiley Interdiscip Rev Dev Biol* **1**, 879-902, doi:10.1002/wdev.77 (2012).
77 Ricard-Blum, S. The collagen family. *Cold Spring Harb Perspect Biol* **3**, a004978, doi:10.1101/cshperspect.a004978 (2011).
78 Johnstone, I. L. Cuticle collagen genes. Expression in Caenorhabditis elegans. *Trends Genet* **16**, 21-27, doi:10.1016/s0168-9525(99)01857-0 (2000).
79 Tu, H., Huhtala, P., Lee, H. M., Adams, J. C. & Pihlajaniemi, T. Membrane-associated collagens with interrupted triple-helices (MACITs): evolution from a bilaterian common ancestor and functional conservation in C. elegans. *BMC Evol Biol* **15**, 281, doi:10.1186/s12862-015-0554-3 (2015).
80 Davis, P. *et al.* WormBase in 2022-data, processes, and tools for analyzing Caenorhabditis elegans. *Genetics* **220**, doi:10.1093/genetics/iyac003 (2022).
81 Teuscher, A. C. *et al.* Longevity interventions modulate mechanotransduction and extracellular matrix homeostasis in C. elegans. *Nat Commun* **15**, 276, doi:10.1038/s41467-023-44409-2 (2024).
82 Thacker, C., Sheps, J. A. & Rose, A. M. Caenorhabditis elegans dpy-5 is a cuticle procollagen processed by a proprotein convertase. *Cell Mol Life Sci* **63**, 1193-1204, doi:10.1007/s00018-006-6012-z (2006).

83 Van de Walle, P. *et al.* CEH-60/PBX regulates vitellogenesis and cuticle permeability through intestinal interaction with UNC-62/MEIS in Caenorhabditis elegans. *PLoS Biol* **17**, e3000499, doi:10.1371/journal.pbio.3000499 (2019).
84 Sandhu, A., Badal, D., Sheokand, R., Tyagi, S. & Singh, V. Specific collagens maintain the cuticle permeability barrier in Caenorhabditis elegans. *Genetics* **217**, doi:10.1093/genetics/iyaa047 (2021).
85 Liu, O. W. & Shen, K. The transmembrane LRR protein DMA-1 promotes dendrite branching and growth in C. elegans. *Nat Neurosci* **15**, 57-63, doi:10.1038/nn.2978 (2011).
86 Hess, M., Gomariz, A., Goksel, O. & Ewald, C. Y. In-Vivo Quantitative Image Analysis of Age-Related Morphological Changes of C. elegans Neurons Reveals a Correlation between Neurite Bending and Novel Neurite Outgrowths. *eNeuro* **6**, doi:10.1523/ENEURO.0014-19.2019 (2019).
87 Conte, D., Jr., MacNeil, L. T., Walhout, A. J. M. & Mello, C. C. RNA Interference in Caenorhabditis elegans. *Curr Protoc Mol Biol* **109**, 26 23 21-26 23 30, doi:10.1002/0471142727.mb2603s109 (2015).
88 Thein, M. C. *et al.* Caenorhabditis elegans exoskeleton collagen COL-19: an adult-specific marker for collagen modification and assembly, and the analysis of organismal morphology. *Dev Dyn* **226**, 523-539, doi:10.1002/dvdy.10259 (2003).
89 Ewald, C. Y., Landis, J. N., Porter Abate, J., Murphy, C. T. & Blackwell, T. K. Dauer-independent insulin/IGF-1-signalling implicates collagen remodelling in longevity. *Nature* **519**, 97-101, doi:10.1038/nature14021 (2015).
90 Zhu, Y., Li, W., Dong, Y., Xia, C. & Fu, R. Hemidesmosomes Sense Collagen Damage to Trigger Innate Immune Response in the Epidermis. *Cells* **12**, doi:10.3390/cells12182223 (2023).
91 Dodd, W. *et al.* A Damage Sensor Associated with the Cuticle Coordinates Three Core Environmental Stress Responses in. *Genetics* **208**, 1467-1482, doi:10.1534/genetics.118.300827 (2018).
92 Corsi, A. K., Wightman, B. & Chalfie, M. A Transparent window into biology: A primer on Caenorhabditis elegans. *WormBook*, 1-31, doi:10.1895/wormbook.1.177.1 (2015).
93 Hobert, O. The neuronal genome of Caenorhabditis elegans. *WormBook*, 1-106, doi:10.1895/wormbook.1.161.1 (2013).
94 Rozario, T. & DeSimone, D. W. The extracellular matrix in development and morphogenesis: a dynamic view. *Dev Biol* **341**, 126-140, doi:10.1016/j.ydbio.2009.10.026 (2010).
95 Ramirez-Suarez, N. J. *et al.* Axon-Dependent Patterning and Maintenance of Somatosensory Dendritic Arbors. *Dev Cell* **48**, 229-244.e224, doi:10.1016/j.devcel.2018.12.015 (2019).
96 Liang, X., Dong, X., Moerman, D. G., Shen, K. & Wang, X. Sarcomeres Pattern Proprioceptive Sensory Dendritic Endings through UNC-52/Perlecan in C. elegans. *Dev Cell* **33**, 388-400, doi:10.1016/j.devcel.2015.03.010 (2015).
97 Taylor, S. R. *et al.* Molecular topography of an entire nervous system. *Cell* **184**, 4329-4347.e4323, doi:10.1016/j.cell.2021.06.023 (2021).
98 Babu, K., Hu, Z., Chien, S. C., Garriga, G. & Kaplan, J. M. The immunoglobulin super family protein RIG-3 prevents synaptic potentiation and regulates Wnt signaling. *Neuron* **71**, 103-116, doi:10.1016/j.neuron.2011.05.034 (2011).
99 Oliver, D. *et al.* Integrins Have Cell-Type-Specific Roles in the Development of Motor Neuron Connectivity. *J Dev Biol* **7**, doi:10.3390/jdb7030017 (2019).
100 Rohlfing, A. K., Miteva, Y., Hannenhalli, S. & Lamitina, T. Genetic and physiological activation of osmosensitive gene expression mimics transcriptional signatures of pathogen infection in C. elegans. *PLoS One* **5**, e9010, doi:10.1371/journal.pone.0009010 (2010).

101 Lanoue, V. & Cooper, H. M. Branching mechanisms shaping dendrite architecture. *Dev Biol* **451**, 16-24, doi:10.1016/j.ydbio.2018.12.005 (2019).
102 Pandey, P., Bhardwaj, A. & Babu, K. Regulation of WNT Signaling at the Neuromuscular Junction by the Immunoglobulin Superfamily Protein RIG-3 in Caenorhabditis elegans. *Genetics* **206**, 1521-1534, doi:10.1534/genetics.116.195297 (2017).
103 Schwarz, V., Pan, J., Voltmer-Irsch, S. & Hutter, H. IgCAMs redundantly control axon navigation in Caenorhabditis elegans. *Neural Dev* **4**, 13, doi:10.1186/1749-8104-4-13 (2009).
104 Dickins, E. M. & Salinas, P. C. Wnts in action: from synapse formation to synaptic maintenance. *Front Cell Neurosci* **7**, 162, doi:10.3389/fncel.2013.00162 (2013).
105 Cescon, M., Chen, P., Castagnaro, S., Gregorio, I. & Bonaldo, P. Lack of collagen VI promotes neurodegeneration by impairing autophagy and inducing apoptosis during aging. *Aging (Albany NY)* **8**, 1083-1101, doi:10.18632/aging.100924 (2016).
106 Bergman, E., Ulfhake, B. & Fundin, B. T. Regulation of NGF-family ligands and receptors in adulthood and senescence: correlation to degenerative and regenerative changes in cutaneous innervation. *Eur J Neurosci* **12**, 2694-2706, doi:10.1046/j.1460-9568.2000.00149.x (2000).
107 Sun, J. H. *et al.* Nerve bundle formation during the promotion of peripheral nerve regeneration: collagen VI-neural cell adhesion molecule 1 interaction. *Neural Regen Res* **17**, 1023-1033, doi:10.4103/1673-5374.324861 (2022).
108 Bhardwaj, A., Pandey, P. & Babu, K. Control of Locomotory Behavior of. *Genetics* **214**, 135-145, doi:10.1534/genetics.119.302872 (2020).
109 Cuentas-Condori, A. *et al.* neurons have functional dendritic spines. *Elife* **8**, doi:10.7554/eLife.47918 (2019).
110 Lippman, J. & Dunaevsky, A. Dendritic spine morphogenesis and plasticity. *J Neurobiol* **64**, 47-57, doi:10.1002/neu.20149 (2005).
111 Kasai, H., Matsuzaki, M., Noguchi, J., Yasumatsu, N. & Nakahara, H. Structure-stability-function relationships of dendritic spines. *Trends Neurosci* **26**, 360-368, doi:10.1016/S0166-2236(03)00162-0 (2003).
112 Feng, X. *et al.* Brain regions vulnerable and resistant to aging without Alzheimer's disease. *PLoS One* **15**, e0234255, doi:10.1371/journal.pone.0234255 (2020).
113 Saxena, S. & Caroni, P. Selective neuronal vulnerability in neurodegenerative diseases: from stressor thresholds to degeneration. *Neuron* **71**, 35-48, doi:10.1016/j.neuron.2011.06.031 (2011).
114 Pan, C. L., Peng, C. Y., Chen, C. H. & McIntire, S. Genetic analysis of age-dependent defects of the Caenorhabditis elegans touch receptor neurons. *Proc Natl Acad Sci U S A* **108**, 9274-9279, doi:10.1073/pnas.1011711108 (2011).
115 Toth, M. L. *et al.* Neurite sprouting and synapse deterioration in the aging Caenorhabditis elegans nervous system. *J Neurosci* **32**, 8778-8790, doi:10.1523/JNEUROSCI.1494-11.2012 (2012).
116 Huntley, M. A. *et al.* Genome-Wide Analysis of Differential Gene Expression and Splicing in Excitatory Neurons and Interneuron Subtypes. *J Neurosci* **40**, 958-973, doi:10.1523/JNEUROSCI.1615-19.2019 (2020).
117 Wallace, M. L. *et al.* Anatomical and single-cell transcriptional profiling of the murine habenular complex. *Elife* **9**, doi:10.7554/eLife.51271 (2020).
118 Teuscher, A. C. *et al.* The CeCoIDB. *Matrix Biol Plus* **1**, 100001, doi:10.1016/j.mbplus.2018.11.001 (2019).
119 Brenner, S. The genetics of Caenorhabditis elegans. *Genetics* **77**, 71-94, doi:10.1093/genetics/77.1.71 (1974).

120 Wang, H., Zhao, Y. & Zhang, Z. Age-dependent effects of floxuridine (FUdR) on senescent pathology and mortality in the nematode Caenorhabditis elegans. *Biochem Biophys Res Commun* **509**, 694-699, doi:10.1016/j.bbrc.2018.12.161 (2019).
121 Glenn, C. F. *et al.* Behavioral deficits during early stages of aging in Caenorhabditis elegans result from locomotory deficits possibly linked to muscle frailty. *J Gerontol A Biol Sci Med Sci* **59**, 1251-1260, doi:10.1093/gerona/59.12.1251 (2004).
122 Berkowitz, L. A., Knight, A. L., Caldwell, G. A. & Caldwell, K. A. Generation of stable transgenic C. elegans using microinjection. *J Vis Exp*, doi:10.3791/833 (2008).
123 Kim, E., Sun, L., Gabel, C. V. & Fang-Yen, C. Long-term imaging of Caenorhabditis elegans using nanoparticle-mediated immobilization. *PLoS One* **8**, e53419, doi:10.1371/journal.pone.0053419 (2013).
124 Clark, S. G. & Chiu, C. C. elegans ZAG-1, a Zn-finger-homeodomain protein, regulates axonal development and neuronal differentiation. *Development* **130**, 3781-3794, doi:10.1242/dev.00571 (2003).
125 Chalfie, M. & Sulston, J. Developmental genetics of the mechanosensory neurons of Caenorhabditis elegans. *Dev Biol* **82**, 358-370, doi:10.1016/0012-1606(81)90459-0 (1981).
126 Li, W., Kang, L., Piggott, B. J., Feng, Z. & Xu, X. Z. The neural circuits and sensory channels mediating harsh touch sensation in Caenorhabditis elegans. *Nat Commun* **2**, 315, doi:10.1038/ncomms1308 (2011).
127 Driscoll, M. & Chalfie, M. The mec-4 gene is a member of a family of Caenorhabditis elegans genes that can mutate to induce neuronal degeneration. *Nature* **349**, 588-593, doi:10.1038/349588a0 (1991).
128 Ly, K., Reid, S. J. & Snell, R. G. Rapid RNA analysis of individual Caenorhabditis elegans. *MethodsX* **2**, 59-63, doi:10.1016/j.mex.2015.02.002 (2015).
129 Henderson, S. T. & Johnson, T. E. daf-16 integrates developmental and environmental inputs to mediate aging in the nematode Caenorhabditis elegans. *Curr Biol* **11**, 1975-1980, doi:10.1016/s0960-9822(01)00594-2 (2001).
130 Edgar, R., Domrachev, M. & Lash, A. E. Gene Expression Omnibus: NCBI gene expression and hybridization array data repository. *Nucleic Acids Res* **30**, 207-210, doi:10.1093/nar/30.1.207 (2002).
131 Barrett, T. *et al.* NCBI GEO: archive for functional genomics data sets--update. *Nucleic Acids Res* **41**, D991-995, doi:10.1093/nar/gks1193 (2013).
132 Kanehisa, M. & Goto, S. KEGG: kyoto encyclopedia of genes and genomes. *Nucleic Acids Res* **28**, 27-30, doi:10.1093/nar/28.1.27 (2000).
133 Huang, D. W. *et al.* DAVID Bioinformatics Resources: expanded annotation database and novel algorithms to better extract biology from large gene lists. *Nucleic Acids Res* **35**, W169-175, doi:10.1093/nar/gkm415 (2007).
134 Sherman, B. T. *et al.* DAVID: a web server for functional enrichment analysis and functional annotation of gene lists (2021 update). *Nucleic Acids Res* **50**, W216-W221, doi:10.1093/nar/gkac194 (2022).

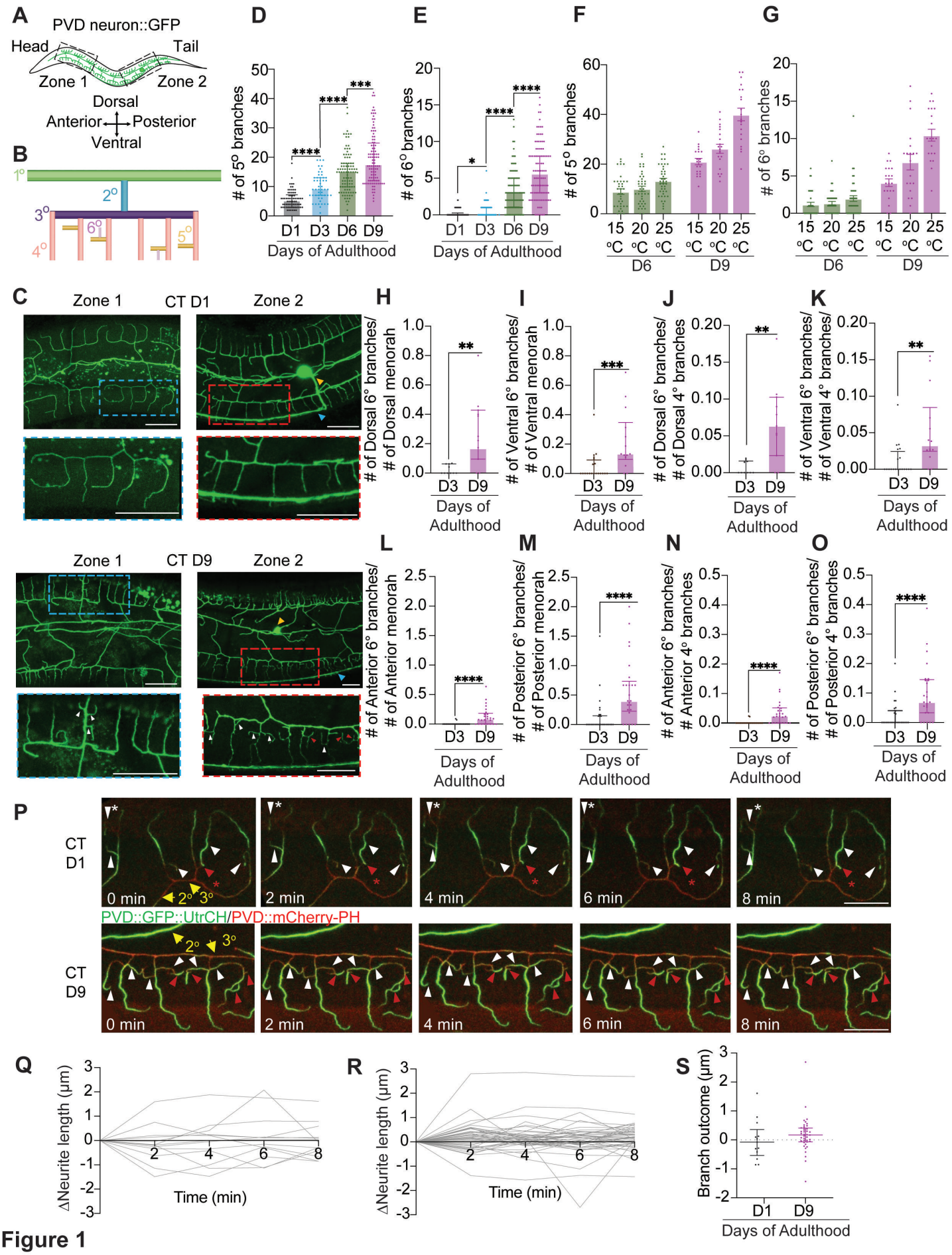
A
PVD neuron::GFP
Head
Tail
Zone 1
Zone 2
Dorsal
Anterior
Posterior
Ventral
B
1°
2°
3°
4°
5°
6°
D
# of 5° branches
D1 D3 D6 D9
Days of Adulthood
E
# of 6° branches
D1 D3 D6 D9
Days of Adulthood
F
# of 5° branches
15 °C 20 °C 25 °C
D6
D9
G
# of 6° branches
15 °C 20 °C 25 °C
D6
D9
C
Zone 1
CT D1
Zone 2
Zone 1
CT D9
Zone 2
H
# of Dorsal 6° branches/ # of Dorsal menorah
D3 D9
Days of Adulthood
I
# of Ventral 6° branches/ # of Ventral menorah
D3 D9
Days of Adulthood
J
# of Dorsal 6° branches/ # of Dorsal 4° branches
D3 D9
Days of Adulthood
K
# of Ventral 6° branches/ # of Ventral 4° branches/
D3 D9
Days of Adulthood
L
# of Anterior 6° branches/ # of Anterior menorah
D3 D9
Days of Adulthood
M
# of Posterior 6° branches/ # of Posterior menorah
D3 D9
Days of Adulthood
N
# of Anterior 6° branches/ # Anterior 4° branches
D3 D9
Days of Adulthood
O
# of Posterior 6° branches/ # of Posterior 4° branches
D3 D9
Days of Adulthood
P
CT D1
0 min
2 min
4 min
6 min
8 min
PVD::GFP::UtrCH/PVD::mCherry-PH
CT D9
0 min
2 min
4 min
6 min
8 min
Q
ΔNeurite length (µm)
Time (min)
R
ΔNeurite length (µm)
Time (min)
S
Branch outcome (µm)
D1 D9
Days of Adulthood

Figure 1

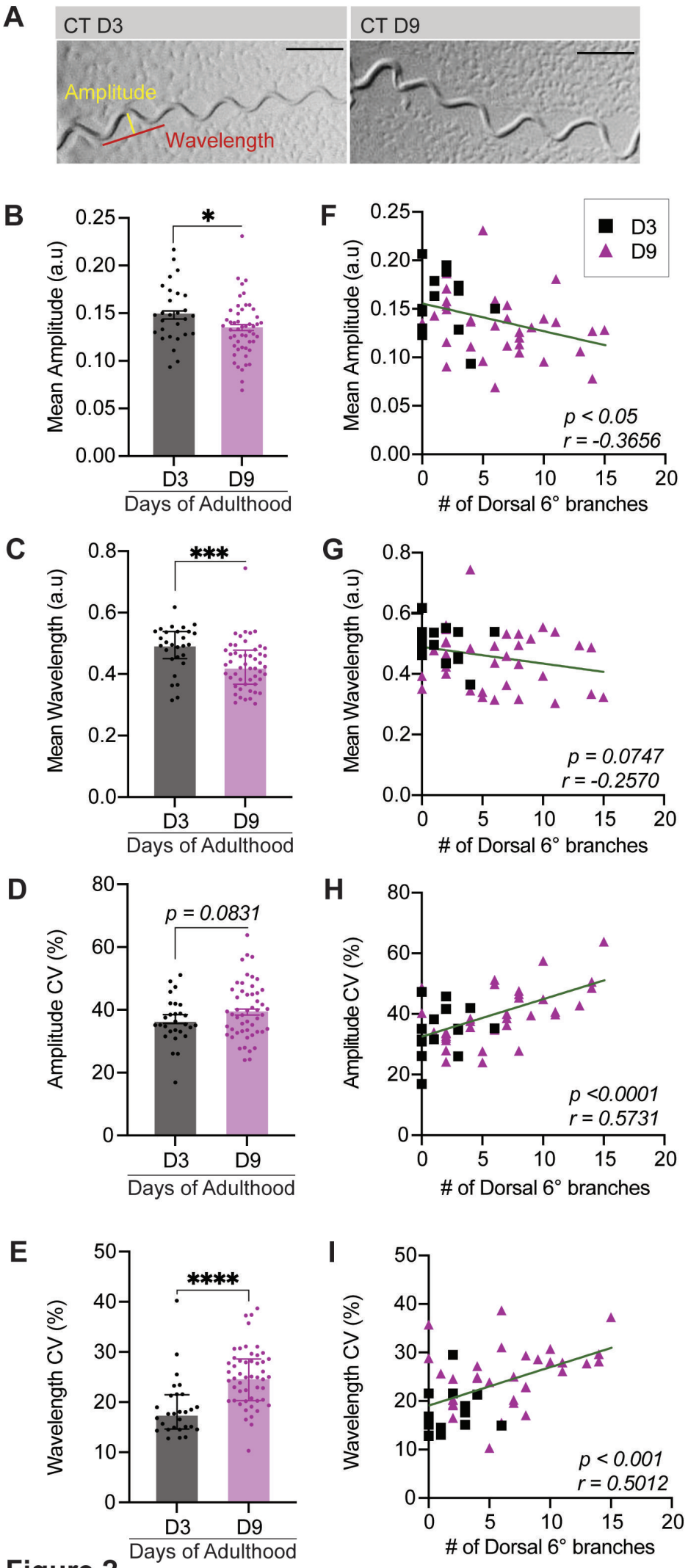
A
CT D3
CT D9
Amplitude
Wavelength
B
Mean Amplitude (a.u)
0.25
0.20
0.15
0.10
0.05
0.00
*
D3
D9
Days of Adulthood
F
Mean Amplitude (a.u)
D3
D9
p < 0.05
r = -0.3656
0
5
10
15
20
# of Dorsal 6° branches
C
Mean Wavelength (a.u)
0.8
0.6
0.4
0.2
0.0
***
D3
D9
Days of Adulthood
G
Mean Wavelength (a.u)
p = 0.0747
r = -0.2570
# of Dorsal 6° branches
D
Amplitude CV (%)
80
60
40
20
0
p = 0.0831
D3
D9
Days of Adulthood
H
Amplitude CV (%)
p <0.0001
r = 0.5731
# of Dorsal 6° branches
E
Wavelength CV (%)
50
40
30
20
10
0
****
D3
D9
Days of Adulthood
I
Wavelength CV (%)
p < 0.001
r = 0.5012
# of Dorsal 6° branches

Figure 2

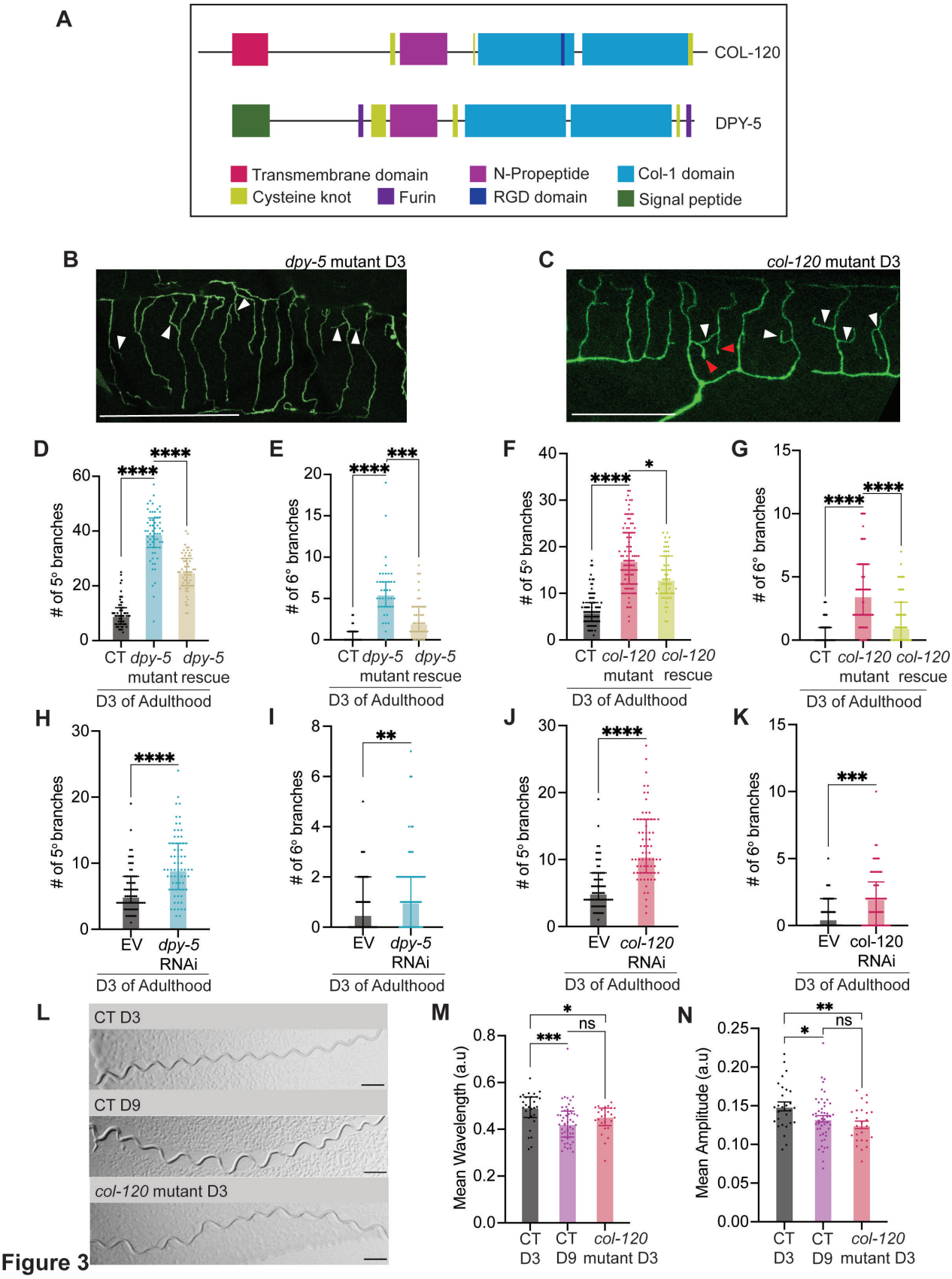
A
COL-120
DPY-5
Transmembrane domain
Cysteine knot
Furin
N-Propeptide
RGD domain
Col-1 domain
Signal peptide
B
dpy-5 mutant D3
C
col-120 mutant D3
D
# of 5° branches
CT
dpy-5 mutant
dpy-5 rescue
D3 of Adulthood
E
# of 6° branches
F
col-120 mutant
col-120 rescue
G
H
EV
dpy-5 RNAi
I
J
col-120 RNAi
K
L
CT D3
CT D9
col-120 mutant D3
M
Mean Wavelength (a.u)
ns
N
Mean Amplitude (a.u)

Figure 3

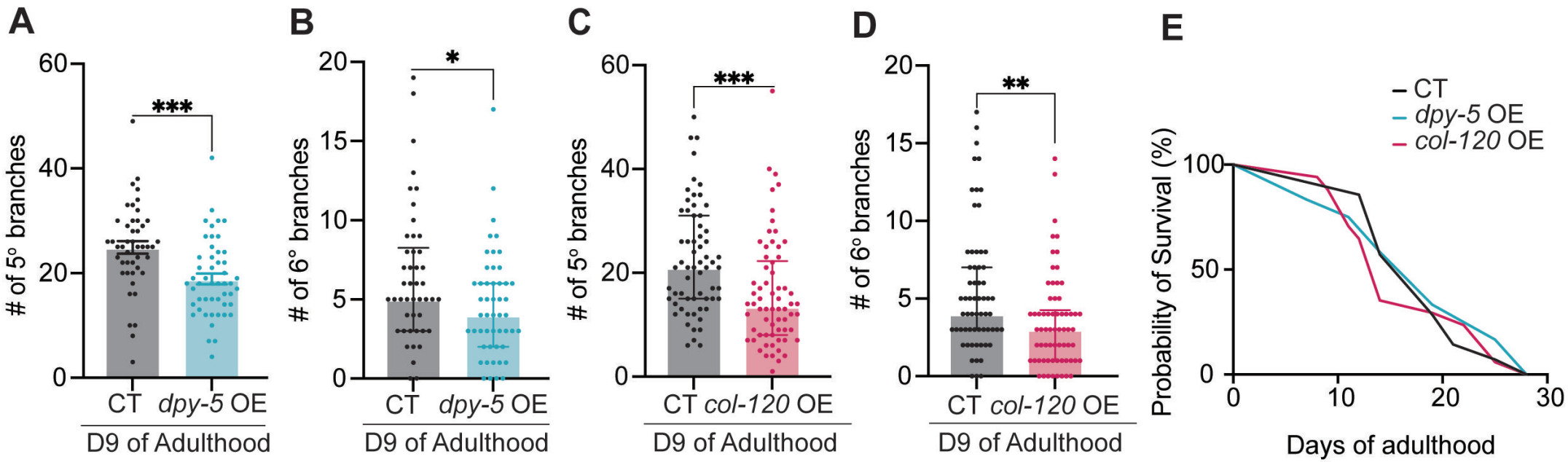
A
B
C
D
E
# of 5° branches
# of 6° branches
***
*
**
CT
dpy-5 OE
col-120 OE
D9 of Adulthood
Probability of Survival (%)
Days of adulthood

Figure 4

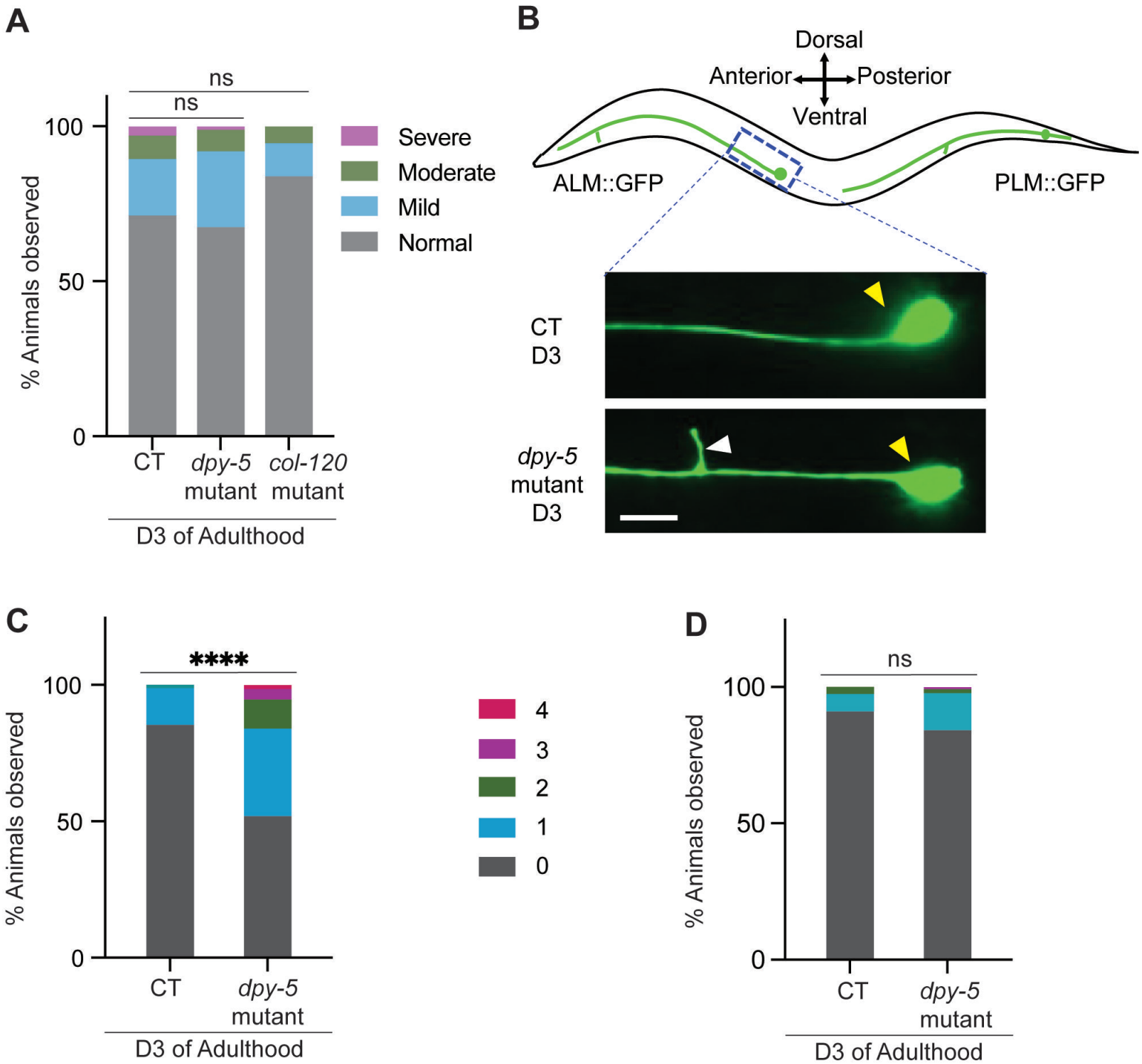
A
ns
ns
100
50
0
% Animals observed
Severe
Moderate
Mild
Normal
CT
dpy-5 mutant
col-120 mutant
D3 of Adulthood
B
Dorsal
Anterior
Posterior
Ventral
ALM::GFP
PLM::GFP
CT D3
dpy-5 mutant D3
C
****
100
50
0
% Animals observed
4
3
2
1
0
CT
dpy-5 mutant
D3 of Adulthood
D
ns
100
50
0
% Animals observed
CT
dpy-5 mutant
D3 of Adulthood

Figure 5

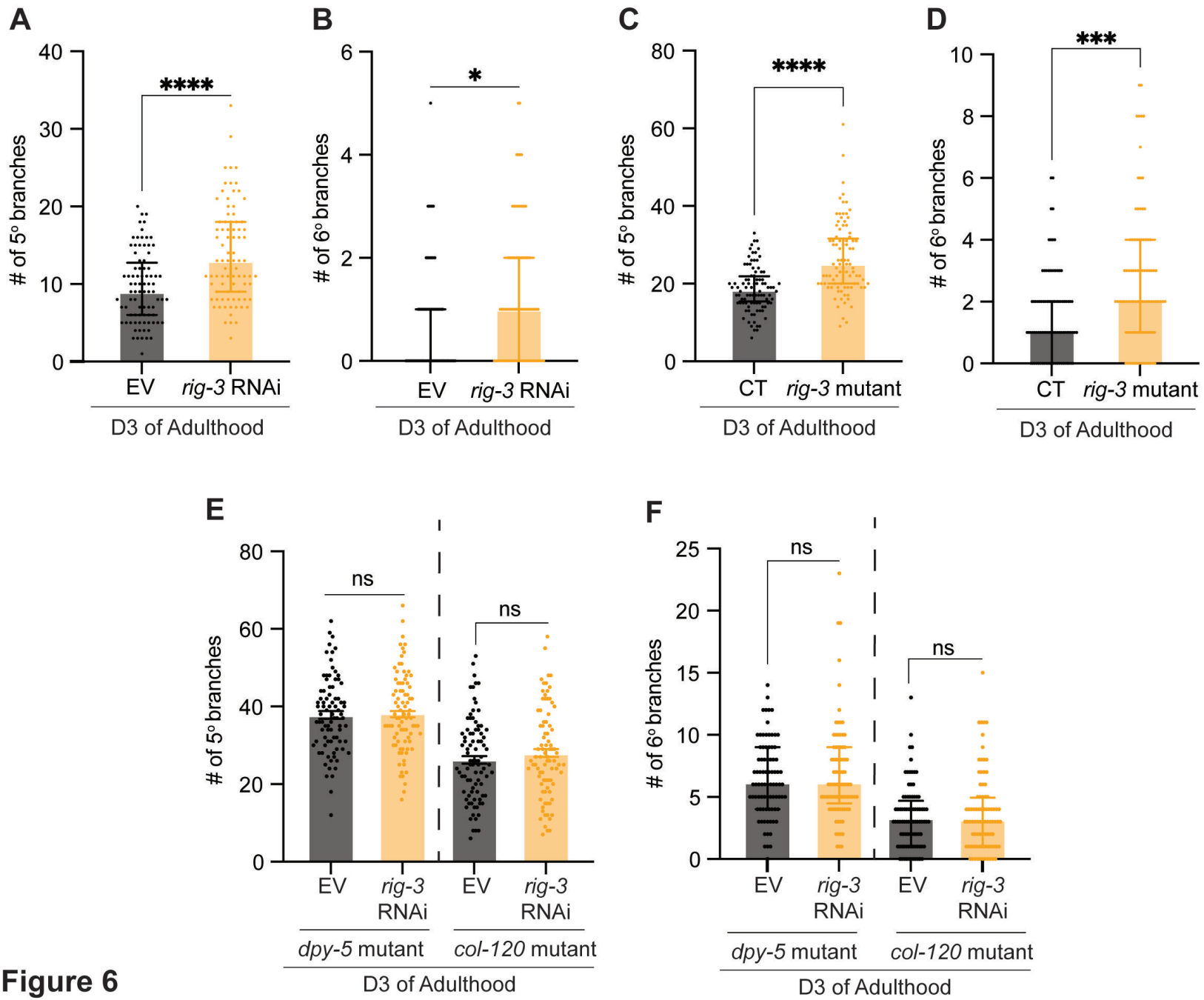
A
B
C
D
E
F
# of 5° branches
# of 6° branches
****
*
***
ns
EV
rig-3 RNAi
CT
rig-3 mutant
dpy-5 mutant
col-120 mutant
D3 of Adulthood

Figure 6

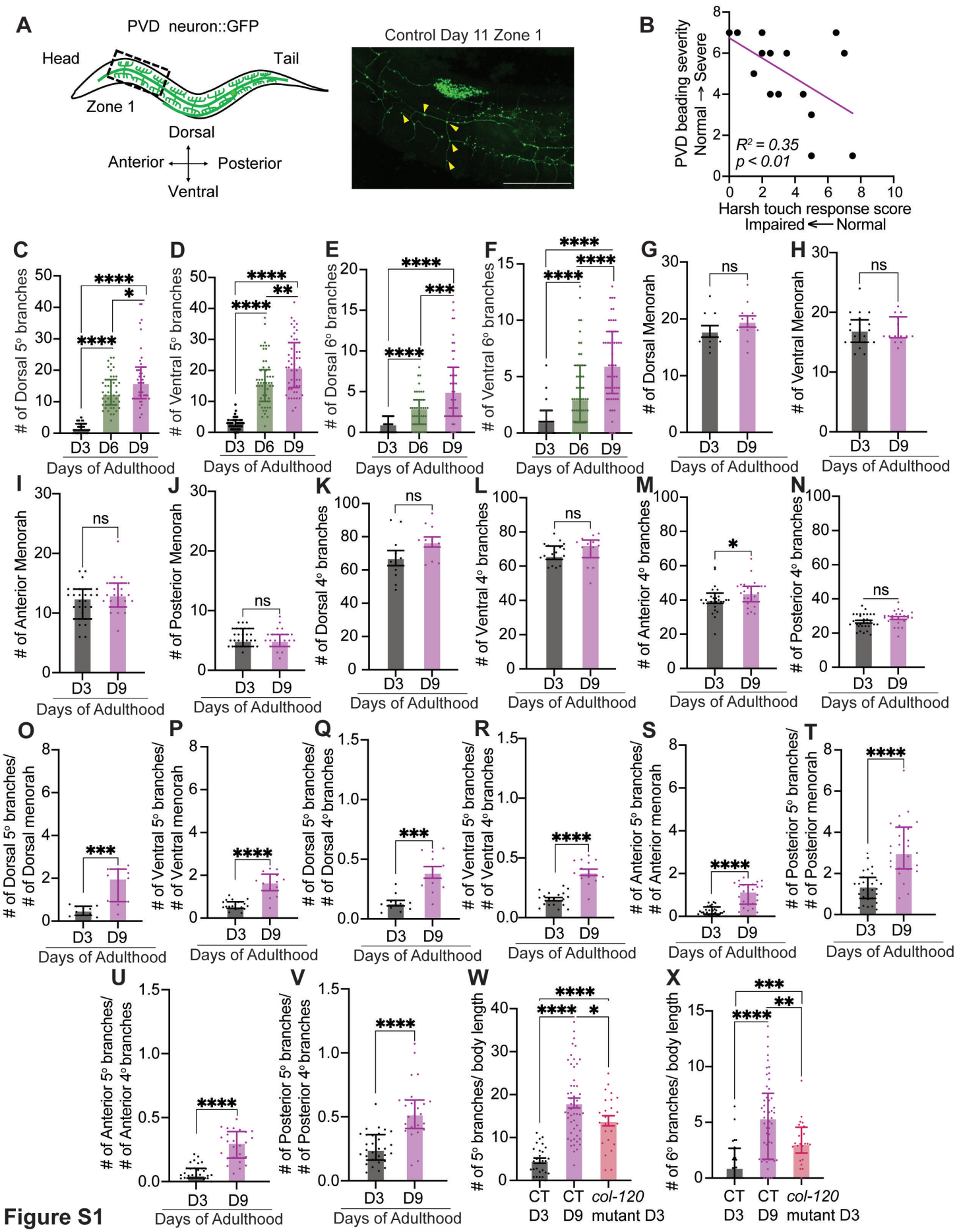
A
PVD neuron::GFP
Head
Tail
Zone 1
Dorsal
Anterior
Posterior
Ventral
Control Day 11 Zone 1
B
PVD beading severity
Normal → Severe
R² = 0.35
p < 0.01
Harsh touch response score
Impaired ← Normal
C
# of Dorsal 5° branches
D
# of Ventral 5° branches
E
# of Dorsal 6° branches
F
# of Ventral 6° branches
G
# of Dorsal Menorah
H
# of Ventral Menorah
I
# of Anterior Menorah
J
# of Posterior Menorah
K
# of Dorsal 4° branches
L
# of Ventral 4° branches
M
# of Anterior 4° branches
N
# of Posterior 4° branches
O
# of Dorsal 5° branches/ # of Dorsal menorah
P
# of Ventral 5° branches/ # of Ventral menorah
Q
# of Dorsal 5° branches/ # of Dorsal 4° branches
R
# of Ventral 5° branches/ # of Ventral 4° branches
S
# of Anterior 5° branches/ # of Anterior menorah
T
# of Posterior 5° branches/ # of Posterior menorah
U
# of Anterior 5° branches/ # of Anterior 4° branches
V
# of Posterior 5° branches/ # of Posterior 4° branches
W
# of 5° branches/ body length
X
# of 6° branches/ body length
D3
D6
D9
Days of Adulthood
ns
CT D3
CT D9
col-120 mutant D3

Figure S1

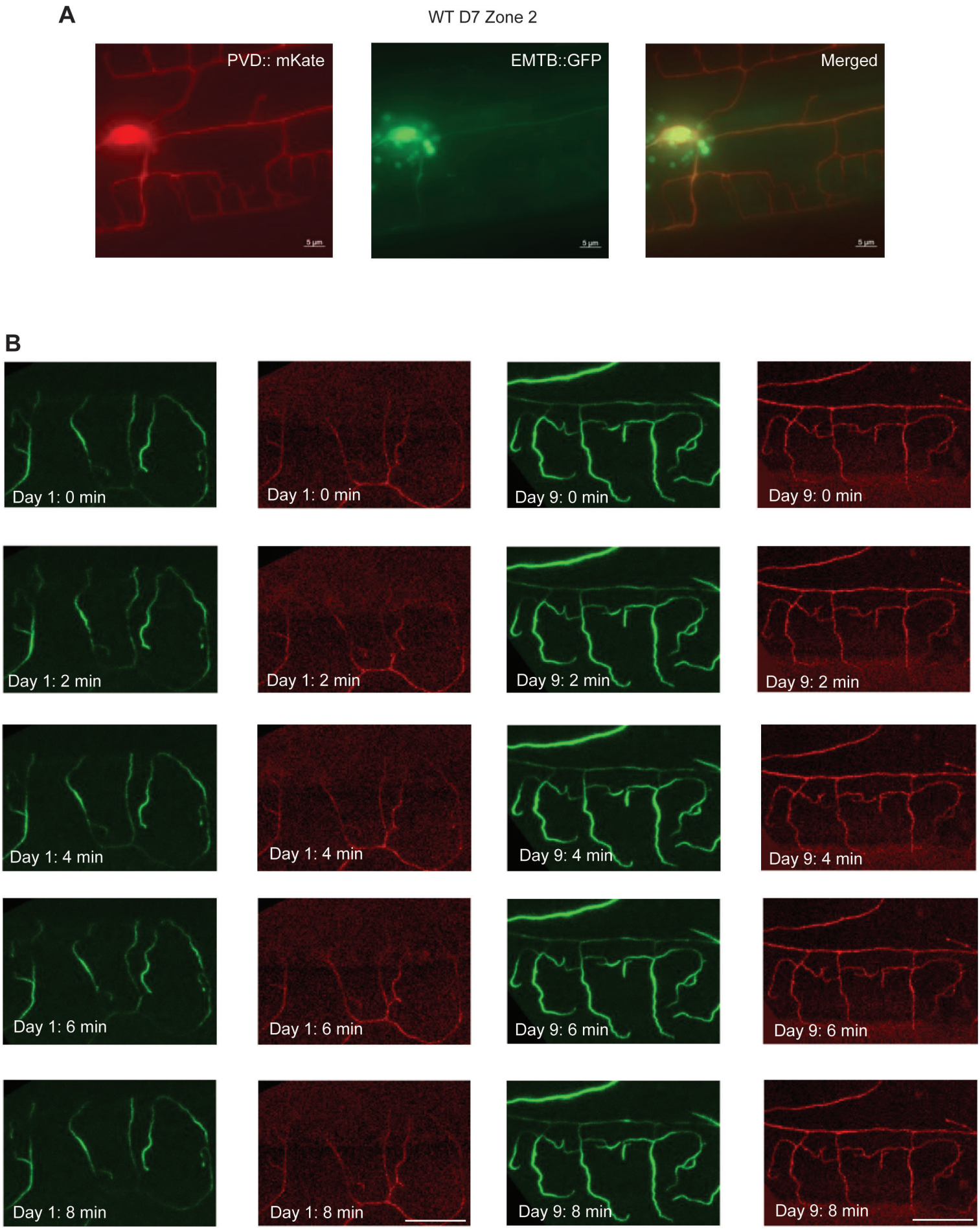
A
WT D7 Zone 2
PVD:: mKate
EMTB::GFP
Merged
B
Day 1: 0 min
Day 1: 0 min
Day 9: 0 min
Day 9: 0 min
Day 1: 2 min
Day 1: 2 min
Day 9: 2 min
Day 9: 2 min
Day 1: 4 min
Day 1: 4 min
Day 9: 4 min
Day 9: 4 min
Day 1: 6 min
Day 1: 6 min
Day 9: 6 min
Day 9: 6 min
Day 1: 8 min
Day 1: 8 min
Day 9: 8 min
Day 9: 8 min

Figure S2

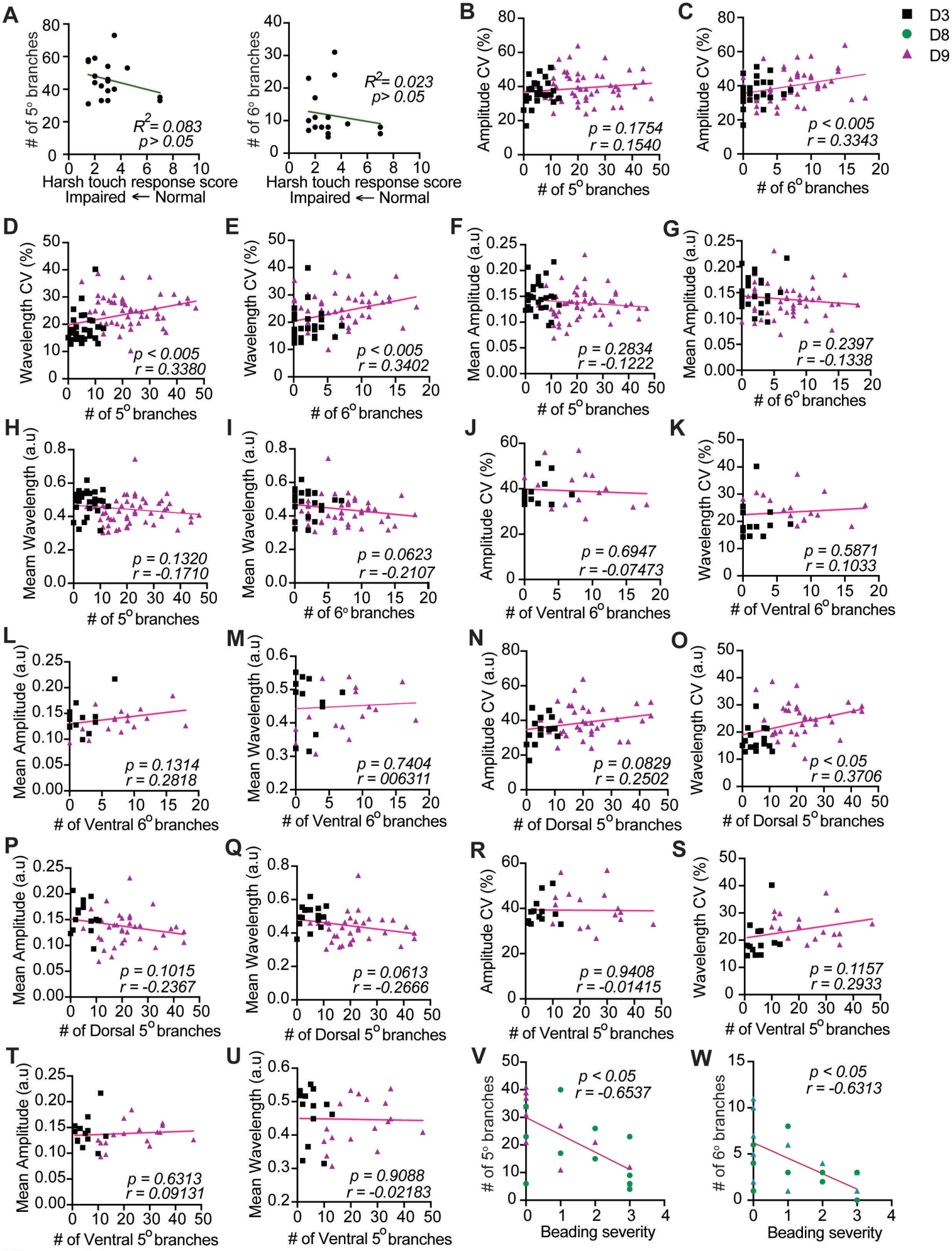
A
# of 5° branches
Harsh touch response score
Impaired ← Normal
R2= 0.083
p> 0.05
# of 6° branches
R2= 0.023
p> 0.05
B
Amplitude CV (%)
# of 5° branches
p = 0.1754
r = 0.1540
C
Amplitude CV (%)
# of 6° branches
p < 0.005
r = 0.3343
D3
D8
D9
D
Wavelength CV (%)
# of 5° branches
p < 0.005
r = 0.3380
E
Wavelength CV (%)
# of 6° branches
p < 0.005
r = 0.3402
F
Mean Amplitude (a.u)
# of 5° branches
p = 0.2834
r = -0.1222
G
Mean Amplitude (a.u)
# of 6° branches
p = 0.2397
r = -0.1338
H
Meam Wavelength (a.u)
# of 5° branches
p = 0.1320
r = -0.1710
I
Mean Wavelength (a.u)
# of 6° branches
p = 0.0623
r = -0.2107
J
Amplitude CV (%)
# of Ventral 6° branches
p = 0.6947
r = -0.07473
K
Wavelength CV (%)
# of Ventral 6° branches
p = 0.5871
r = 0.1033
L
Mean Amplitude (a.u)
# of Ventral 6° branches
p = 0.1314
r = 0.2818
M
Mean Wavelength (a.u)
# of Ventral 6° branches
p = 0.7404
r = 006311
N
Amplitude CV (a.u)
# of Dorsal 5° branches
p = 0.0829
r = 0.2502
O
Wavelength CV (a.u)
# of Dorsal 5° branches
p < 0.05
r = 0.3706
P
Mean Amplitude (a.u)
# of Dorsal 5° branches
p = 0.1015
r = -0.2367
Q
Mean Wavelength (a.u)
# of Dorsal 5° branches
p = 0.0613
r = -0.2666
R
Amplitude CV (%)
# of Ventral 5° branches
p = 0.9408
r = -0.01415
S
Wavelength CV (%)
# of Ventral 5° branches
p = 0.1157
r = 0.2933
T
Mean Amplitude (a.u)
# of Ventral 5° branches
p = 0.6313
r = 0.09131
U
Mean Wavelength (a.u)
# of Ventral 5° branches
p = 0.9088
r = -0.02183
V
# of 5° branches
Beading severity
p < 0.05
r = -0.6537
W
# of 6° branches
Beading severity
p < 0.05
r = -0.6313

Figure S3

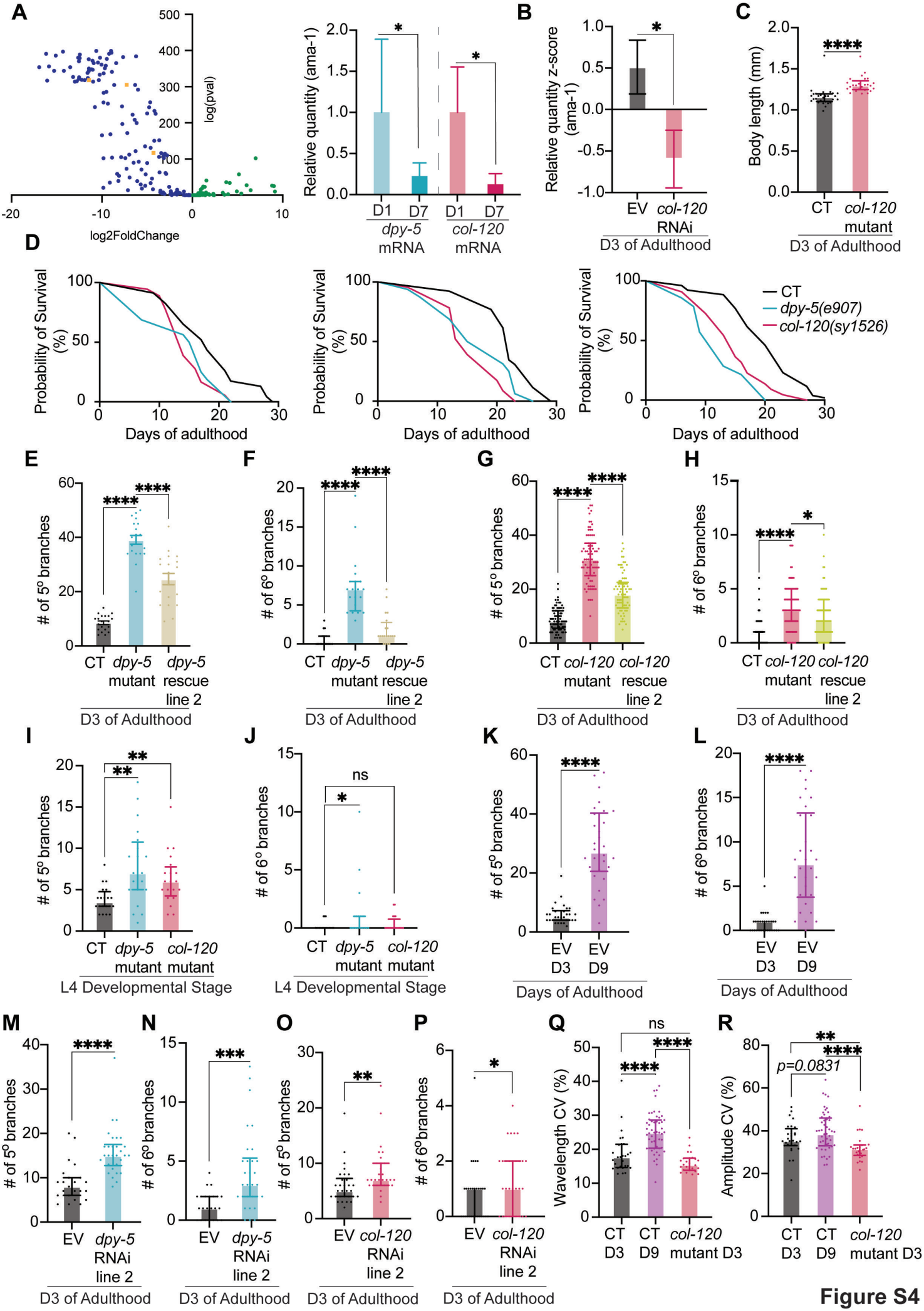
A
log(pval)
log2FoldChange
Relative quantity (ama-1)
D1 D7 D1 D7
dpy-5 mRNA
col-120 mRNA
B
Relative quantity z-score (ama-1)
EV col-120 RNAi
D3 of Adulthood
C
Body length (mm)
CT col-120 mutant
D3 of Adulthood
D
Probability of Survival (%)
Days of adulthood
CT
dpy-5(e907)
col-120(sy1526)
E
# of 5° branches
CT dpy-5 mutant dpy-5 rescue line 2
D3 of Adulthood
F
# of 6° branches
CT dpy-5 mutant dpy-5 rescue line 2
D3 of Adulthood
G
# of 5° branches
CT col-120 mutant col-120 rescue line 2
D3 of Adulthood
H
# of 6° branches
CT col-120 mutant col-120 rescue line 2
D3 of Adulthood
I
# of 5° branches
CT dpy-5 mutant col-120 mutant
L4 Developmental Stage
J
# of 6° branches
ns
CT dpy-5 mutant col-120 mutant
L4 Developmental Stage
K
# of 5° branches
EV D3 EV D9
Days of Adulthood
L
# of 6° branches
EV D3 EV D9
Days of Adulthood
M
# of 5° branches
EV dpy-5 RNAi line 2
D3 of Adulthood
N
# of 6° branches
EV dpy-5 RNAi line 2
D3 of Adulthood
O
# of 5° branches
EV col-120 RNAi line 2
D3 of Adulthood
P
# of 6° branches
EV col-120 RNAi line 2
D3 of Adulthood
Q
ns
Wavelength CV (%)
CT D3 CT D9 col-120 mutant D3
R
p=0.0831
Amplitude CV (%)
CT D3 CT D9 col-120 mutant D3

Figure S4

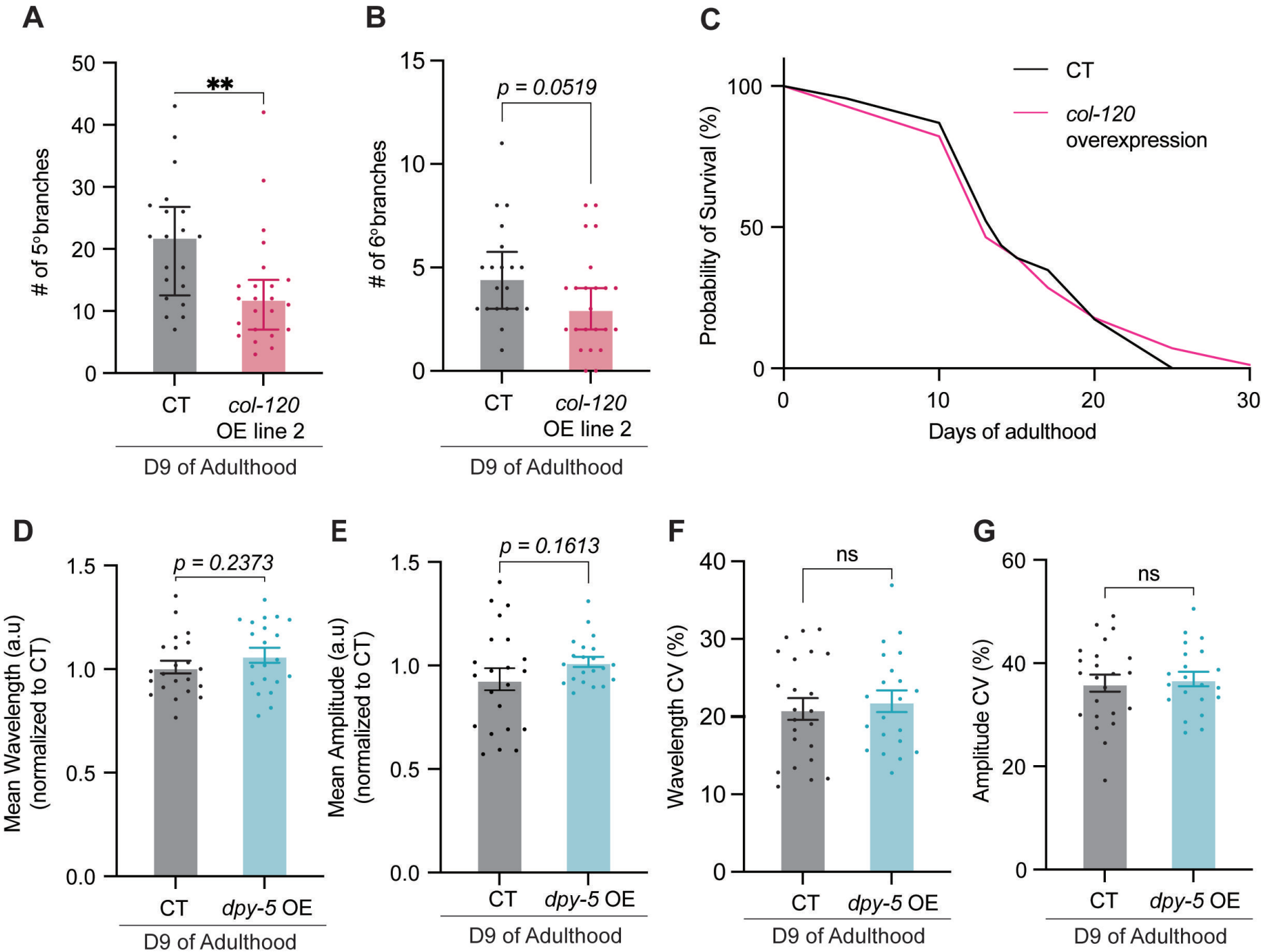
A
50
40
30
20
10
0
# of 5° branches
**
CT
col-120
OE line 2
D9 of Adulthood
B
15
10
5
0
# of 6° branches
p = 0.0519
CT
col-120
OE line 2
D9 of Adulthood
C
100
50
0
Probability of Survival (%)
CT
col-120
overexpression
0
10
20
30
Days of adulthood
D
1.5
1.0
0.5
0.0
Mean Wavelength (a.u)
(normalized to CT)
p = 0.2373
CT
dpy-5 OE
D9 of Adulthood
E
1.5
1.0
0.5
0.0
Mean Amplitude (a.u)
(normalized to CT)
p = 0.1613
CT
dpy-5 OE
D9 of Adulthood
F
40
30
20
10
0
Wavelength CV (%)
ns
CT
dpy-5 OE
D9 of Adulthood
G
60
40
20
0
Amplitude CV (%)
ns
CT
dpy-5 OE
D9 of Adulthood

Figure S5

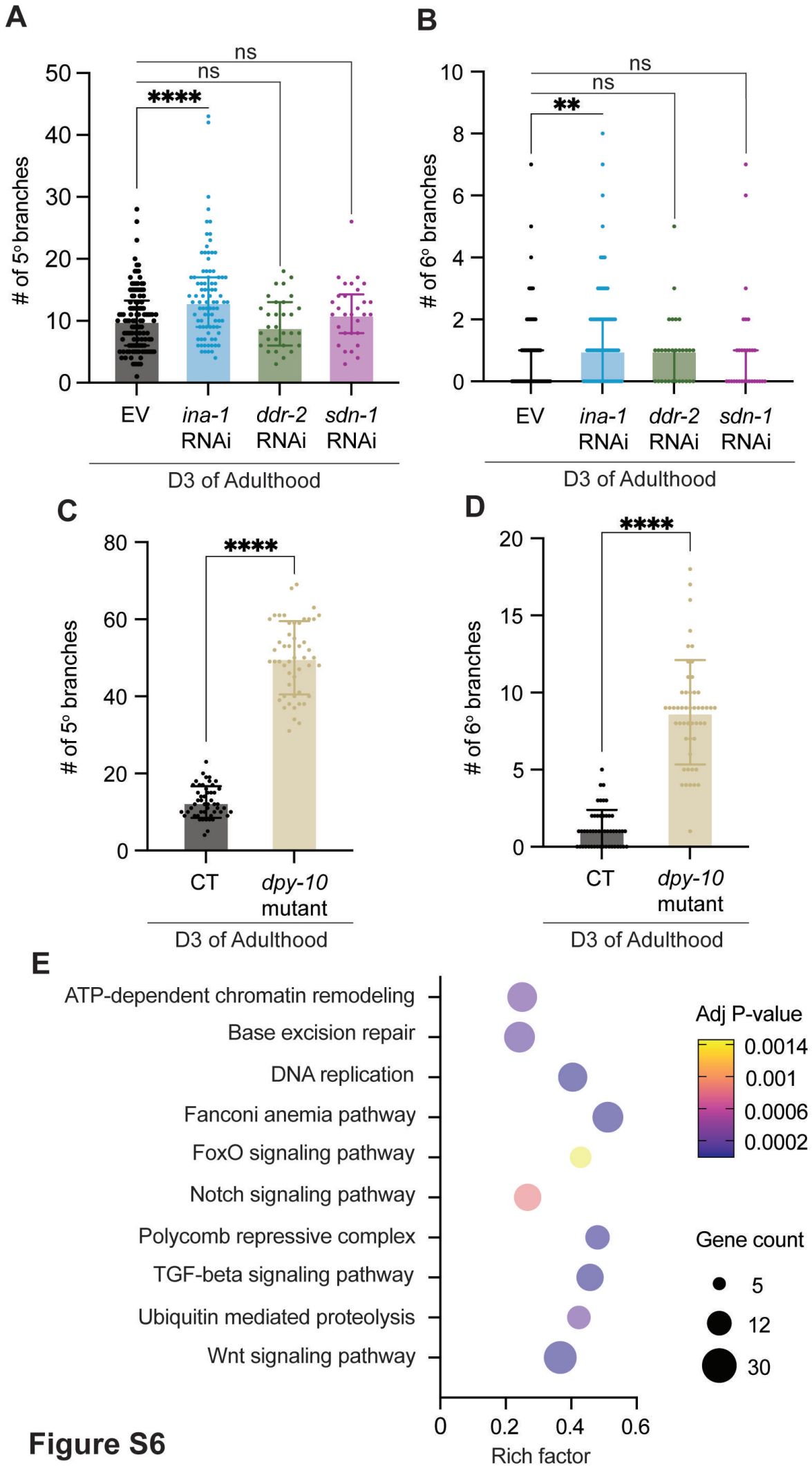
A
ns
ns
****
# of 5° branches
50
40
30
20
10
0
EV
ina-1 RNAi
ddr-2 RNAi
sdn-1 RNAi
D3 of Adulthood
B
ns
ns
**
# of 6° branches
10
8
6
4
2
0
EV
ina-1 RNAi
ddr-2 RNAi
sdn-1 RNAi
D3 of Adulthood
C
****
# of 5° branches
80
60
40
20
0
CT
dpy-10 mutant
D3 of Adulthood
D
****
# of 6° branches
20
15
10
5
0
CT
dpy-10 mutant
D3 of Adulthood
E
ATP-dependent chromatin remodeling
Base excision repair
DNA replication
Fanconi anemia pathway
FoxO signaling pathway
Notch signaling pathway
Polycomb repressive complex
TGF-beta signaling pathway
Ubiquitin mediated proteolysis
Wnt signaling pathway
0
0.2
0.4
0.6
Rich factor
Adj P-value
0.0014
0.001
0.0006
0.0002
Gene count
5
12
30

Figure S6

Supplemental Table 1

Difference	Right 5th branches	Left 5th branches	Right 6th branches	Left 6th branches
WT D3 vs WT D6	+14 ****	+10 ****	+2 ****	+1 ***
WT D6 vs WT D9	+3.208 *	+4 *	+3.5 ****	+3.5 ****
WT D3 vs WT D9	+18 ****	+14 ****	+4.5 ****	+4.5 ****

Supplemental Table 2

Difference	Dorsal 5th branches	Ventral 5th branches	Dorsal 6th branches	Ventral 6th branches
dpy-5 mutant D3 vs WT D3	+26.5 ****	+23 ****	+5 ****	+7 ****
dpy-5 mutant D3 vs WT D3	+13.5 ****	+15.5 ****	+1 ****	+3 ****
dpy-5 overexpression D9 vs WT D9	-7.19 *	-8 *	-1 ns	-1 p = 0.0547
col-120 overexpression D9 vs WT D9	-8.5 *	-8.5 *	-0.5 ns	-2 *
dpy-5 RNAi D3 vs EV D3	+5 ****	+5 *	+1 *	+0.5 ns
col-120 RNAi D3 vs EV D3	+4 ****	+8 ****	+1 ns	+1 *